Integrated Sensing and Communications for V2I Networks: Dynamic Predictive Beamforming for Extended Vehicle Targets

Zhen Du, *Graduate Student Member, IEEE*, Fan Liu, *Member, IEEE*, Weijie Yuan, *Member, IEEE*, Christos Masouros, *Senior Member, IEEE*, Zenghui Zhang, *Senior Member, IEEE*, Shuqiang Xia, and Giuseppe Caire, *Fellow, IEEE*

Abstract—We investigate sensing-assisted beamforming for vehicle-to-infrastructure (V2I) communication by exploiting integrated sensing and communications (ISAC) functionalities at the roadside unit (RSU). The RSU deploys a massive multi-input-multi-output (mMIMO) array at mmWave. The pencil-sharp mMIMO beams and fine range-resolution implicate that the point-target assumption is impractical, as the vehicle's geometry becomes essential. Therefore, the communication receiver (CR) may never lie in the beam, even when the vehicle is accurately tracked. To tackle this problem, we consider the extended target with two novel schemes. For the first scheme, the beamwidth is adjusted in real-time to cover the entire vehicle, followed by an extended Kalman filter to predict and track the position of CR according to resolved scatterers. An upgraded scheme is proposed by splitting each transmission block into two stages. The first stage is exploited for ISAC with a wide beam. Based on the sensed results at the first stage, the second stage is dedicated to communication with a pencil-sharp beam, yielding significant communication improvements. We reveal the inherent tradeoff between the two stages in terms of their durations, and develop an optimal allocation strategy that maximizes the average achievable rate. Finally, simulations verify the superiorities of proposed schemes over state-of-the-art methods.

Index Terms—integrated sensing and communication, extended target tracking, MIMO beamforming, V2I

Zhen Du is with the School of Electronic and Information Engineering, Nanjing University of Information Science and Technology, Nanjing 210044, China, and is also with the Department of Electronic and Electrical Engineering, Southern University of Science and Technology, Shenzhen 518055, China. (email: duzhen@nuist.edu.cn).

Fan Liu and Weijie Yuan are with the Department of Electronic and Electrical Engineering, Southern University of Science and Technology, Shenzhen 518055, China (email: liuf6@sustech.edu.cn; yuanwj@sustech.edu.cn).

Christos Masouros is with the Department of Electronic and Electrical Engineering, University College London, London WC1E 7JE, U.K. (email: chris.masouros@ieee.org)

Zenghui Zhang is with the School of Electronic Information and Electrical Engineering, Shanghai Jiao Tong University, Shanghai 200240, China (email: zenghui.zhang@sjtu.edu.cn).

Shuqiang Xia is with ZTE Corporation, Shenzhen, China, and is also with State Key Laboratory of Mobile Network and Mobile Multimedia Technology, Shenzhen 518055, China (email: xia.shuqiang@zte.com.cn).

Giuseppe Caire is with the Electrical Engineering and Computer Science Department, Technische Universität Berlin, 10587 Berlin, Germany (email: caire@tuberlin.de).

I. INTRODUCTION

The intelligent transportation system (ITS) has been playing an increasingly important role in building smart cities, which requires the information interaction among vehicles, pedestrians, obstacles, and infrastructures [2]–[4]. To achieve such a goal, vehicle-to-everything (V2X) communication has become a key technique in ITS, which is currently supported by two potential technologies: dedicated short-range communications (DSRC) [5] and Cellular V2X (C-V2X) [6], [7]. However, DSRC can not meet the demand of the high data traffic, particularly in high vehicle density scenarios [8]. Besides, conventional C-V2X schemes such as LTE-V2X can only provide localization services at the accuracy of $10m$ and latency of $1s$ [9]. This is unable to meet the critical demand of future V2X networks, requiring high-accuracy localization services on the order of a centimeter and latency on the order of a millisecond in high-mobility scenarios [10].

Fortunately, the state-of-the-art V2X communication is supported by the fifth-generation (5G) communication techniques, and in particular, the mMIMO and mmWave technologies [10]. Moreover, the potential functionality of wireless sensing is envisioned as an important enabler in numerous emerging applications [11]–[14]. To be specific, by exploiting the mMIMO antenna array pencil-sharp beams can be generated, to compensate for the mmWave propagation path loss, providing large array gain while improving the angular resolution for vehicle sensing. Moreover, both communication rate and ranging resolution are significantly improved, thanks to the large bandwidth at the mmWave band. Critically, the sparsity of mmWave channel enables the much fewer Non Line-of-Sight (NLoS) components relative to the sub-6 GHz band, which is in favor of the vehicle localization [10]. Featured with the above attributes, it is sought to equip the V2X network with both sensing and communication capabilities, such that the vehicles can better interact with surroundings to realize driving safety. In consideration of all these perspectives, recent efforts have been taken towards the feasibility of integrated sensing and communications (ISAC) in V2X networks [15]–[20].

More relevant to this work, a mmWave vehicle-to-infrastructure (V2I) mmWave communication scenario is considered in [15], where the roadside unit (RSU) is equipped with a dedicated radar sensor to aid the communication

beamforming. Such a scheme leads to the more precise V2I beam alignment while reducing the beam training overheads, whereas at the cost of extra hardwares. To further exploit the performance gain of sensing-assisted communication in V2X networks, [16] proposed an ISAC approach to use the mmWave ISAC signaling for predictive beamforming in high mobility V2I scenarios. The echo of the downlink signal reflected from the vehicle is collected for estimating the vehicle's state parameters (distance, velocity, angle of arrival, radar cross section, etc) with matched-filtering [21] at the current time instant. Then an extended Kalman filtering (EKF) approach is exploited to predict the position of vehicle so as to accurately align the beam. The benefit of this methodology is that the predictive beamforming is achieved without extra devices, i.e., a single signal is exploited to realize two functionalities of communications and sensing. Further, [17] approached the same objective from a Bayesian perspective and utilized the message passing algorithm, which provides an enhanced tracking performance over the EKF algorithm used in [16]. Overall, in contrast to the conventional beam training [22], [23] or beam tracking [24], [25] which are built upon 5G new radio (NR) protocol [26, Chap.9], the advantages of the sensing-assisted beam tracking with the ISAC signaling can be summarized as follows:

- Pilot overheads of 5G NR protocol-based beam training/tracking, which refer to the channel-state-information reference signals (CSI-RS), and uplink feedbacks, can be released [11], [16], [26]. Conventional beam training or beam tracking demands the RSU to transmit pilots ahead of each data block in the downlink channel. Then the vehicle can estimate the state information and feed it back to the RSU in the uplink channel. Sensing-assisted beam tracking can release such high overheads burden[1], as shown in Fig. 1. Note that pilot overheads of demodulation reference signal (DM-RS) are still necessary for channel estimation and coherent demodulation in the communication receiver (CR);

- Significant matched-filtering gain [11]. For conventional beam training or beam tracking, only a very limited number of pilots are used. On the contrary, the ISAC approach exploits the whole data frame for both sensing and communication. As such, and despite the echo power attenuation caused by the round-trip path loss, the matched filtering gain of sensing is much more significant. As a result, the state estimation can be more precise due to the higher receive signal-to-noise ratio (SNR);

- The extra ranging information on top of the angle estimation provides additional degrees of freedom (DoFs) for more accurately localizing the vehicle. This forms the basis of this paper where a dynamic beamwidth is determined by the angle and the distance simultaneously.

The aforementioned works are dedicated to handling beam tracking of point-like vehicles. In practical scenarios, however, the vehicle as a target may be extended in both range and angle

[1]If the ISAC beam tracking loses the trajectory, CSI-RS and uplink feedbacks are needed for a resetting to recover the target.
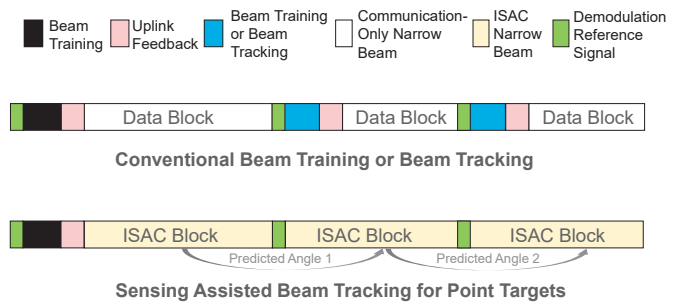

Fig. 1. Frame structures of the conventional beam traning/tracking method and sensing-assisted beam tracking for point targets method.
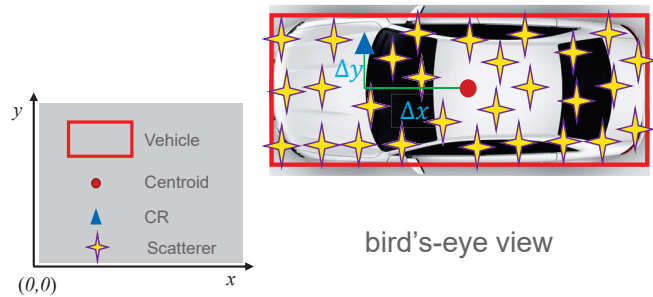

Fig. 2. A schematic diagram of the extended target vehicle with multiple uniformly distributed scatterers.

domains, and the precise position of the CR in the vehicle is key in beam tracking. Consequently, the approaches discussed in [16]–[20] may suffer from significant performance loss, and even fail to provide a reliable V2I link. As an example, a 128-antenna mMIMO array is able to synthesize a pencil-sharp beam, with a beamwidth at the order of $1°$-$2°$. This suggests that, when treating it as a point-like target, the vehicle is unlikely to be entirely illuminated by the narrow beam, especially when it approaches the illuminator, i.e., the RSU in our case. Owing to this reason, even if the vehicle can be accurately tracked, the position of CR deployed on the vehicle may be beyond the effective region of beamwidth, resulting in beam misalignment and link outages. Moreover, the 5G mmWave signaling occupies a bandwidth up to the order of GHz, indicating that the vehicle may be distributed in multiple range cells (e.g., for a bandwidth of $B = 500$MHz, the range resolution is $c/(2B) = 3e^8/(2 \times 5e^8) = 30cm$ [21], where c is the speed of light). In others words, even if the CR is in the effective beamwidth at present, the point-like modeling does not allow the high-resolution sensing to locate the correct range cell that the CR lies in. Therefore, the wrong range cell as the input to the beam tracker may lead to considerable tracking errors.

To overcome the above challenges, we propose the sensing-assisted predictive beam tracking in V2I networks by modeling the vehicle as an extended target. The major novelties of this article can be summarized in accordance with the proposed two schemes:

- **ISAC-based predictive beam tracking with dynamic beam (ISAC-DB):** Inspired by the geometry of the

extended vehicle target with multiple resolvable scatterers as shown in Fig. 2, the coordinates of the CR can be inferred according to measured state vectors of all scatterers. Subsequently, the beam alignment can be performed using a tailored EKF algorithm. In contrast to [16] where a pencil-sharp beam with fixed beamwidth is generated to track a point-like vehicle target, in this work the beamwidth must be adjusted in real-time in accordance with the predicted distance and the angle of CR to illuminate the entire vehicle.

- **ISAC-based predictive beam tracking with alternant wide beam and narrow beam (ISAC-AB):** When the vehicle approaches the RSU, fewer antennas enlarging the beamwidth brings forth the declining array gain, resulting in decreased achievable rate. Motivated by this observation, a more advanced scheme is proposed by splitting each block into two parts. The first part is used for ISAC transmission, which has a dynamic beamwidth following ISAC-DB. The second part is dedicated to the communication performance, and transmitted on a narrow beam formulated by leveraging the estimated results from the first part. This results in a remarkable improvement in the achievable rate. Moreover, the inherent tradeoff between these two parts is revealed by a convex optimization model, where a time allocation strategy between the two stages is developed to optimize the average transmission rate.

The numerical results demonstrate that the proposed two schemes are capable of handling effective beam alignment, and providing more stable and reliable communication transmission over the conventional methods. It is worth highlighting that the more advanced ISAC-AB can attain excellent achievable rate in V2I networks.

The remainder of this article is organized as follows. Section II introduces the system modeling, Section III elaborates the proposed two schemes for beam tracking, Section IV provides the simulations, and finally Section VI concludes the article.

Notation: Throughout this paper, $\mathbf{A}$, $\mathbf{a}$, and a denote matrix, vector, and scalar, respectively. $(\cdot)^T$, $(\cdot)^H$, $(\cdot)^{-1}$, $|\cdot|$, $\lfloor\cdot\rfloor$, $E(\cdot)$, $\mathbf{0}_N$, and $\mathbf{I}_N$ denote transpose, Hermitian, inverse, modulus of a complex number, equal to or smaller than a real number, expectation, zero vector of size $N \times 1$, and identity matrix of size $N \times N$, respectively. $\arctan^{-1}(\cdot)$ denotes inverse tangent function in radian. Besides, $\mathcal{N}(\boldsymbol{\mu}, \mathbf{R})$ denotes Gaussian distribution with mean $\boldsymbol{\mu}$ and covariance matrix $\mathbf{R}$, while $\mathcal{CN}(\boldsymbol{\mu}, \mathbf{R})$ represents circularly symmetric complex Gaussian distribution with mean $\boldsymbol{\mu}$ and covariance matrix $\mathbf{R}$. Finally, $\mathbb{C}^{N \times M}$ denotes the complex space of dimension $N \times M$.

II. SYSTEM MODELING

We consider a V2I downlink where a full-duplex RSU supports both sensing and data transmission. The RSU operates at the mmWave band and is equipped with mMIMO uniform linear array (ULA) which has $N_{t,n}$ transmit antennas and N_r receive antennas[2]. The subscript of $N_{t,n}$ indicates that it

[2]In practice, the RSU is installed with a known height, and the pitch angle is thus known *a priori*. Hence, the considered 2D scenario with the ULA can be readily extended to the 3D case with the uniform plane array (UPA) [27].

may change at different epochs n on account of the varying beamwidth, which is distinctly different from many previous works like [16]–[20]. As for the vehicle, it moves along a straight road, which is parallel to the ULA. The extension to a non-parallel case is straightforward by rotating the coordinate system. The vehicle is modeled as an extended target equipped with a single-antenna CR. Resolvable scatterers are uniformly distributed in the vehicle geometry. Hence, once the coordinates of these scatterers are localized, the coordinates of centroid can be uniquely determined. Accordingly, the position of CR would be inferred since its relative coordinates to the centroid can be known *a priori*.

Without loss of generality, denote the angle, the distance and the velocity of the vehicle's CR relative to the RSU's array by $\phi(t)$, $d(t)$ and $v(t)$. All these motion parameters are defined in the region $t \in [0, T]$, with T being the maximum time duration of interest. In the tracking procedure, we discretize the time period T into several small time-slots with a duration of ΔT. Further, denote the motion parameters at the nth epoch by ϕ_n, d_n and v_n, where $\phi_n = \phi(n\Delta T)$, $d_n = d(n\Delta T)$ and $v_n = v(n\Delta T)$. Note that the predictive beamforming is conducted once within each interval of ΔT. To ensure there is no *range migration* so that the well-known "stop-go" radar model [21] can be used, $v_n \Delta T \le \Delta r = \frac{c}{2B}$ must be satisfied, where Δr and B denote the range resolution and the bandwidth, respectively. For instance, mmWave signaling occupies a large bandwidth of 500MHz and a high mobility vehicle moves in the speed of $20m/s$, then $\Delta T < 0.015s$ is parameterized.

A. Radar Signal Model

At the nth epoch, the RSU receives the echo contributed by the vehicle's K resolved scatterers with N_r receive antennas, expressed as

$$
\begin{aligned}
\mathbf{r}_n(t) = \kappa_n \sqrt{p_n} \sum_{k=1}^{K} \beta_{k,n} e^{j2\pi\mu_{k,n}t} \mathbf{b}\left(\theta_{k,n}\right) \mathbf{a}_n^H\left(\theta_{k,n}\right) \\
\times \mathbf{f}_n s_n\left(t - \tau_{k,n}\right) + \mathbf{z}_r(t),
\end{aligned}
\tag{1}
$$

where $\mathbf{r}_n(t) \in \mathbb{C}^{N_r \times 1}$; $\kappa_n = \sqrt{N_{t,n} N_r}$ is the array gain factor; p_n denotes the transmitted power; $\mu_{k,n}$, $\beta_{k,n}$ and $\tau_{k,n}$ denote the Doppler frequency, the complex reflection coefficient and the round-trip delay of the kth scatterer at the nth epoch, respectively; $s_n(t)$ is the transmitted ISAC signal; $\mathbf{z}_r(t) \in \mathbb{C}^{N_r \times 1}$ represents the complex additive white Gaussian noise with zero mean and variance of σ^2, i.e., $\mathbf{z}_r(t) \sim \mathcal{CN}(\mathbf{0}_{N_r}, \sigma^2 \mathbf{I}_{N_r \times 1})$. Herein, the transmit SNR is defined as $\frac{p_n}{\sigma^2}$.

Besides, $\mathbf{a}_n(\theta)$ and $\mathbf{b}(\theta)$ are transmit and receive steering vectors of the RSU's ULA, in the forms of

$$
\mathbf{a}_n(\theta) = \frac{1}{\sqrt{N_{t,n}}} \left[1, e^{-j\pi\cos\theta}, \cdots, e^{-j\pi(N_{t,n}-1)\cos\theta}\right]^T, \tag{2}
$$

$$
\mathbf{b}(\theta) = \frac{1}{\sqrt{N_r}} \left[1, e^{-j\pi\cos\theta}, \cdots, e^{-j\pi(N_r-1)\cos\theta}\right]^T, \tag{3}
$$

where a standard half-wavelength antenna spacing for the ULA is assumed, and $\theta \in (0, \pi)$. Here, we emphasize that $\mathbf{a}_n(\theta)$ depends on $N_{t,n}$, which indicates that its size may change at

different epochs due to the varying $N_{t,n}$. The beamforming vector $\mathbf{f}_n$ is designed by exploiting the predicted angle of the CR, given as

$$\mathbf{f}_n = \mathbf{a}_n\left(\widehat{\phi}_{n|n-1}\right), \tag{4}$$

where $\mathbf{f}_n \in \mathbb{C}^{N_{t,n}\times 1}$ is dynamic since the size of $N_{t,n}$ is adjustable. Here, $\widehat{\phi}_{n|n-1}$ denotes the predicted angle of the CR at the nth epoch based on the $(n-1)$th measurement. Throughout this paper, we aim to estimate and predict the angle ϕ_n of the CR[3], so as to steer the beam accurately and guarantee a reliable communication performance.

B. Radar Measurement Model

First, we aim to determine the resolved ranges and velocities in the delay-Doppler domain by following a standard matched-filtering technique [16]. Then the refined output at the RSU is expressed as

$$\begin{aligned}
\widetilde{\mathbf{r}}_n =& \kappa_n\sqrt{p_n}\sum_{k=1}^{K}\beta_{k,n}\mathbf{b}\left(\theta_{k,n}\right)\mathbf{a}_n^H\left(\theta_{k,n}\right)\mathbf{a}_n\left(\widehat{\phi}_{n|n-1}\right) \\
& \times \int_0^{\Delta T} s_n\left(t-\tau_{k,n}\right)s_n^*\left(t-\tau\right)e^{-j2\pi(\mu-\mu_{k,n})t}dt + \widetilde{\mathbf{z}}_r \\
=& \kappa_n\sqrt{p_n}\sqrt{G}\sum_{k=1}^{K}\beta_{k,n}\mathbf{b}\left(\theta_{k,n}\right)\mathbf{a}_n^H\left(\theta_{k,n}\right)\mathbf{a}_n\left(\widehat{\phi}_{n|n-1}\right) \\
& \times \bar{\delta}\left(\tau-\tau_{k,n};\mu-\mu_{k,n}\right) + \widetilde{\mathbf{z}}_r,
\end{aligned} \tag{5}$$

where $\bar{\delta}(\tau;\mu)$ is the normalized matched-filtering output function obtained by time and frequency-reversing and conjugating its own waveform for the complex transmit signal $s_n(t)$ [28]. Notice that $\bar{\delta}(\tau;\mu)$ generally has a narrow-mainlobe property both in delay domain and Doppler domain to ensure high distance and velocity resolution, and $\bar{\delta}(\tau;\mu)=1$ when $\tau=0$ and $\mu=0$. The usage of matched-filtering enables the receive SNR of sensing to improve by a matched-filtering gain denoted as G. Note that G is equal to the number of symbols used for matched-filtering in a block. Besides, $\widetilde{\mathbf{z}}_r$ represents the noise output of matched-filtering. Hence, the delay and Doppler of the kth scatterer can be readily measured by finding the location of the corresponding peak position, expressed as

$$\widehat{\tau}_{k,n} = \frac{2d_{k,n}}{c} + z_{\tau_{k,n}}, \ \ \widehat{\mu}_{k,n} = \frac{2v_n\cos(\theta_{k,n})f_c}{c} + z_{\mu_{k,n}}. \tag{6}$$

Definition: In consideration of the radar signal with a large bandwidth, a narrow mainlobe of matched-filtering output function corresponds to a high range resolution. The kth and the k'th scatterers $(k, k' = 1, 2, \cdots, K$ and $k \neq k')$ are said to be separable in the time-delay axis, if the time difference of arrival between them satisfies

$$\left|\tau_{k,n} - \tau_{k',n}\right| > \tau_0, \tag{7}$$

where τ_0 is the effective mainlobe duration of the matched-filtering output function in time-delay axis (i.e., corresponding to the range resolution Δr). An example of matched-filtering
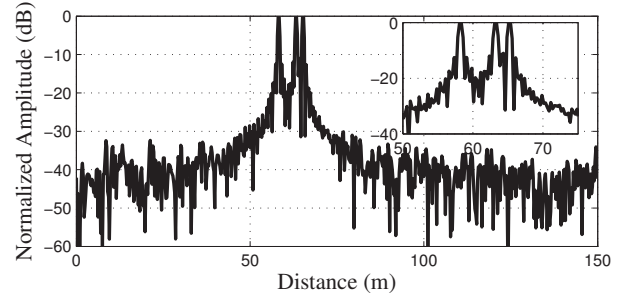
Fig. 3. An example of matched-filtering output in the distance profiles. The signaling bandwidth is 500MHz and the scenario contains three scatterers with distances as $(58, 63, 65)m$, respectively.

output is shown in Fig. 3, where three scatterers are separable since their distance differences are larger than Δr. In the Doppler domain there is a similar definition, which is omitted here for notational convenience.

For the kth scatterer, substituting $\tau = \widehat{\tau}_{k,n}$ and $\mu = \widehat{\mu}_{k,n}$ into the matched-filtering output function (5) and relying on the above definition yields

$$\widetilde{\mathbf{r}}_{k,n} = \kappa_n\beta_{k,n}\mathbf{b}\left(\theta_{k,n}\right)\mathbf{a}_n^H\left(\theta_{k,n}\right)\mathbf{a}_n\left(\widehat{\phi}_{n|n-1}\right) + \bar{\mathbf{z}}_r, \tag{8}$$

which indicates that K scatterers are totally separated. Here, $\bar{\mathbf{z}}_r$ denotes the measurement noise normalized by the transmit power p_n and the matched-filtering gain G, which follows $\bar{\mathbf{z}}_r \sim \mathcal{CN}(\mathbf{0}_{N_r}, \sigma_\theta^2\mathbf{I}_{N_r\times 1})$, where $\sigma_\theta^2 = \frac{\sigma^2}{G p_n}$. Besides, the complex reflection coefficient $\beta_{k,n}$ is determined by the signal propagation distance and the radar cross section[4] (RCS) of the vehicle, expressed as

$$\beta_{k,n} = \frac{\varepsilon_{k,n}}{(2d_{k,n})^2} = \frac{\varepsilon_{k,n}}{c^2\tau_{k,n}^2}, \tag{9}$$

where $\varepsilon_{k,n}$ denotes the complex RCS of the kth slowly fluctuated Swerling I-type scatterer [21] at the nth epoch. The above thorough separation among scatterers is on the basis of the assumption that the sidelobes of $\bar{\delta}(t;\mu)$ are negligible. In practice, sidelobes would affect the perfect separation and their influence is not considered in this article. Then $\theta_{k,n}$ can be readily measured by the maximum likelihood estimation (MLE) [29] or super-resolution algorithms like multiple signal classification (MUSIC) [30], whose measurements are expressed as[5]

$$\widehat{\theta}_{k,n} = \theta_{k,n} + z_{\theta_{k,n}}. \tag{10}$$

Note that $z_{\theta_{k,n}}$, $z_{\tau_{k,n}}$ and $z_{\mu_{k,n}}$ are additive noises with zero means and variances of $\sigma_{k,n}^2(1)$, $\sigma_{k,n}^2(2)$ and $\sigma_{k,n}^2(3)$, respectively. Moreover, we remark here that the measurement variances are inversely proportional to the transmit SNR of (1), i.e.,

$$\sigma_{k,n}^2(i) = \frac{a_i^2\sigma^2}{p_n G|\kappa_n\beta_{k,n}|^2\left|\varrho_{k,n}\right|^2}, \ i = 1, 2, 3. \tag{11}$$

where $\varrho_{k,n} = \mathbf{a}_n^H(\theta_{k,n})\mathbf{a}_n\left(\widehat{\phi}_{n|n-1}\right)$ represents the beamforming gain factor of kth scatterer, whose modulus is less than 1 since the beam points to the CR rather than the kth scatterer. Finally, a_i, $i = 1, 2, 3$ are constants related to the system configuration, signal designs as well as the specific signal processing algorithms [16].

Now, with the measured $\widehat{\tau}_{k,n}$ and $\widehat{\theta}_{k,n}$, the coordinates of vehicle centroid (x_n, y_n) can be localized in the 2D Cartesian coordinate as

$$\widehat{x}_n = \frac{1}{K}\sum_{k=1}^{K} c\widehat{\tau}_{k,n}\cos\widehat{\theta}_{k,n}/2 = \frac{1}{K}\sum_{k=1}^{K}\widehat{d}_{k,n}\cos\widehat{\theta}_{k,n}, \quad (12)$$

$$\widehat{y}_n = \frac{1}{K}\sum_{k=1}^{K} c\widehat{\tau}_{k,n}\sin\widehat{\theta}_{k,n}/2 = \frac{1}{K}\sum_{k=1}^{K}\widehat{d}_{k,n}\sin\widehat{\theta}_{k,n}. \quad (13)$$

Next, we estimate the velocity. Given that

$$\widehat{\mu}_{k,n} = \frac{2v_n\cos(\theta_{k,n})f_c}{c} + z_{\mu_{k,n}}, \ \forall k \quad (14)$$

we reformulate K equations with the matrix-vector form as

$$\widehat{\boldsymbol{\mu}}_n = \mathbf{A}(\boldsymbol{\theta}_n)v_n + \mathbf{z}_\mu, \quad (15)$$

where

- $\widehat{\boldsymbol{\mu}}_n = \left[\widehat{\mu}_{1,n}, \widehat{\mu}_{2,n}, \cdots, \widehat{\mu}_{K,n}\right]^T$,
- $\mathbf{A}(\boldsymbol{\theta}_n) = \left[\frac{2f_c\cos(\theta_{1,n})}{c}, \frac{2f_c\cos(\theta_{2,n})}{c}, \cdots, \frac{2f_c\cos(\theta_{K,n})}{c}\right]^T$,
- $\mathbf{z}_\mu = \left[z_{\mu_{1,n}}, z_{\mu_{2,n}}, \cdots, z_{\mu_{K,n}}\right]^T$.

It is straightforward to see that $\widehat{\boldsymbol{\mu}}_n \sim \mathcal{N}(\mathbf{A}(\boldsymbol{\theta}_n)v_n, \mathbf{Q}_\mu)$, where $\mathbf{Q}_\mu = \mathrm{diag}(\sigma_{1,n}^2(3), \cdots, \sigma_{K,n}^2(3))$. In view of this, the MLE of v_n conditional to $\boldsymbol{\theta}_n$ is thus given as [29]

$$\begin{aligned}\widehat{v}_{n|\boldsymbol{\theta}_n} &= \left(\mathbf{A}^T(\boldsymbol{\theta}_n)\mathbf{Q}_\mu^{-1}\mathbf{A}(\boldsymbol{\theta}_n)\right)^{-1}\mathbf{A}^T(\boldsymbol{\theta}_n)\mathbf{Q}_\mu^{-1}\widehat{\boldsymbol{\mu}}_n \\ &= \frac{c}{2f_c}\cdot\frac{\sum_{k=1}^{K}\widehat{\mu}_{k,n}\cos(\theta_{k,n})/\sigma_{k,n}^2(3)}{\sum_{k=1}^{K}\cos^2(\theta_{k,n})/\sigma_{k,n}^2(3)}.\end{aligned} \quad (16)$$

Assumption: Denote the coordinate of CR as $(x_n + \Delta x, y_n + \Delta y)$ relative to the RSU, where Δx and Δy are relative coordinates of the CR to the centroid. Note that Δx and Δy are known since they can be fed back to the RSU at the initial beam training when the vehicle is captured.

The measurement model is finally summarized as[6]

$$\begin{cases}\widehat{\phi}_n = \tan^{-1}\left(\frac{\widehat{y}_n + \Delta y}{\widehat{x}_n + \Delta x}\right) = \phi_n + z_\phi, \\ \widehat{d}_n = \sqrt{(\widehat{x}_n + \Delta x)^2 + (\widehat{y}_n + \Delta y)^2} = d_n + z_d, \\ \widehat{v}_n = \frac{c}{2f_c}\cdot\frac{\sum_{k=1}^{K}\widehat{\mu}_{k,n}\cos(\widehat{\theta}_{k,n})/\sigma_{k,n}^2(3)}{\sum_{k=1}^{K}\cos^2(\widehat{\theta}_{k,n})/\sigma_{k,n}^2(3)} = v_n + z_v,\end{cases} \quad (17)$$

where z_ϕ, z_d and z_v are measurement noises with zero means and variances of σ_ϕ^2, σ_d^2 and σ_v^2, respectively. In this article, while $\widehat{\theta}_{k,n}$, $\widehat{d}_{k,n}$ and $\widehat{v}_n$ are assumed Gaussian distributed, $\widehat{\phi}_n$, $\widehat{d}_n$ and $\widehat{v}_n$ are not Gaussian due to the non-linearity of (17). Nevertheless, Kalman filter is a linear minimum mean square

---

[6]Note that $\arctan^{-1}(x) \in (-\pi/2, \pi/2)$, while the angle of vehicle is defined in the region of $[0, \pi)$. For clarity, we define $\tan^{-1}(x) = \arctan(x)$ if $x \geq 0$, otherwise $\tan^{-1}(x) = \arctan(x) + \pi$.

error (MMSE) estimator, and hence its performance only depends on second order statistics of the variables involved. Note that Gaussianity is necessary to claim optimality since the linear MMSE estimator is the optimal MMSE estimator only for Gaussian models [31]. Therefore, only means and variances of variables involved are needed to build a Kalman filter. Most of the existing literatures concerning the extended target tracking like [32]–[34] adopts the ideal assumption of known variances of measurement noises. Turning back to our model, σ_ϕ^2, σ_d^2 and σ_v^2 are unknown in practice. To proceed, we develop approaches for obtaining approximate variance counterparts. The detailed derivations are provided in the Appendix.

C. Communication Receiver Model

We emphasize that, the ISAC signal is used for both vehicle tracking and communication transmission during the entire transmission block. Hence, at the nth epoch, the vehicle receives the signal transmitted by the RSU as

$$y_n^C(t) = \alpha_n\kappa_n^C\sqrt{p}\mathbf{a}_n^H(\phi_n)\mathbf{a}_n\left(\widehat{\phi}_{n|n-1}\right)s_n(t) + z_n^C(t). \quad (18)$$

where $\kappa_n^C = \sqrt{N_{t,n}}$ is the array gain. Besides, α_n indicates the LoS channel coefficient, which is given as [35] $\alpha_n = \alpha_{\mathrm{ref}}d_n^{-1}e^{j\frac{2\pi f_c}{c}d_n}$, where $\alpha_{\mathrm{ref}}d_n^{-1}$ is the LoS path-loss of the channel, and α_{ref} is a known reference path-loss measured at the distance of $d_0 = 1m$. Thus, estimating α_n is equivalent to estimating d_n.

The receive SNR of the CR is therefore given as $\mathrm{SNR}_n^C = p_n\left|\kappa_n^C\alpha_n\right|^2\left|\varrho_n^C\right|^2/\sigma_C^2$, where $\varrho_n^C = \mathbf{a}_n^H(\phi_n)\mathbf{a}_n(\widehat{\phi}_{n|n-1})$ represents the beamforming gain factor, whose modulus equals to 1 if the predicted angle perfectly matches the real angle, and is less than 1 otherwise. Clearly, the angle prediction accuracy of CR is predominating in SNR_n^C. Finally, the achievable rate at the nth epoch is formulated as

$$R_n = \log\left(1 + \mathrm{SNR}_n^C\right). \quad (19)$$

Remark 1: The synchronization of the received communication signal can be achieved with pilots at the beginning of the frame structure. Besides, the achievable rate (19) refers to the upper bound of the practical communication rate.

III. ISAC-BASED PREDICTIVE BEAM TRACKING SCHEMES FOR V2I LINKING

As discussed previously, our main focus is to track the CR. For this purpose, the key premise is that the beam must be able to cover the entire vehicle in physical size, in order to cover resolved scatterers as many as possible and to accurately refine the position of centroid. Therefore, the beamwidth must be adjusted in real-time according to the vehicle's trajectory. To this end, we may modify the beamformer by inducing an additional complex weight vector, and its coefficients determine the radiation pattern and in particular the beam shape. As a matter of fact, one can design a codebook of beamforming vectors that generates different beamwidths [36]. As a special case, we can straightforwardly activate different numbers of transmit antennas at the RSU, for a dynamic beampattern with

the varying beamwidth. We refer readers to [37] for a detailed definition of the ULA beamwidth. Here, instead of the first null beamwidth, we resort to the commonly-used half-power beamwidth for the ULA, given as

$$\theta_{BW} = \frac{k_0 c}{N_{t,n} r_0 f_c} \cdot \frac{1}{\sin(\phi)} \approx \frac{1.78}{N_{t,n} \sin(\phi)}, \quad (20)$$

where k_0, r_0, f_c and ϕ denote the beamwidth factor, the ULA spacing, the carrier frequency and the angle of the CR, respectively. Here, the approximation holds when a half wavelength spacing is employed for the ULA.

The coverage width Δd can thus be approximately calculated by a trigonometric function as

$$\Delta d = 2 d_n \cdot \tan\left(\frac{\theta_{BW}}{2}\right) \approx 2 d_n \cdot \tan\left(\frac{0.89}{N_{t,n} \sin(\phi)}\right). \quad (21)$$

In our considered scenario, the vehicular coverage width Δd is assumed to be constant. For example, in terms of a vehicle of the length 5m and the width 2m, the maximum coverage width can be set as $\Delta d > \sqrt{5^2 + 2^2} = 5.385m$.

Moreover, since the beamwidth varies at different epochs, the number of transmit antennas is calculated in terms of (21) based on the predicted $\widehat{d}_{n|n-1}$ and $\widehat{\phi}_{n|n-1}$. Besides, we emphasize that the mMIMO system allows a maximum antenna number as $N_{t,\max}$ (e.g., $N_{t,\max} = 128$). As a consequence, the number of transmit antennas is summarized as

$$N_{t,n} = \min\left\{ \left\lfloor \frac{0.89}{\arctan^{-1}\left(\frac{\Delta d}{2\widehat{d}_{n|n-1}}\right) \cdot \sin(\widehat{\phi}_{n|n-1})} \right\rfloor, N_{t,\max} \right\}. \quad (22)$$

A. ISAC-DB Method

A scenario diagram is illustrated in Fig. 4. At the nth epoch, the state vector is composed of the angle, the distance and the velocity of the CR, given as

$$\mathbf{x}_n = (\phi_n, d_n, v_n)^T. \quad (23)$$

Following the derivation in [16], it is straightforward to summarize the state evolution model of the CR as

$$\begin{cases} \phi_n = \phi_{n-1} + d_{n-1}^{-1} v_{n-1} \Delta T \sin(\phi_{n-1}) + \omega_\phi, \\ d_n = d_{n-1} - v_{n-1} \Delta T \cos(\phi_{n-1}) + \omega_d, \\ v_n = v_{n-1} + \omega_v. \end{cases} \quad (24)$$

The state evolution model and the measurement model are reformulated by more compact matrix-vector forms as

$$\begin{cases} \text{State Evolution Model: } \mathbf{x}_n = \mathbf{h}(\mathbf{x}_{n-1}) + \boldsymbol{\omega}_n, \\ \text{Measurement Model: } \mathbf{y}_n = \mathbf{x}_n + \mathbf{z}_n, \end{cases} \quad (25)$$

where $\mathbf{y}_n = \widehat{\mathbf{x}}_n = [\widehat{\phi}_n, \widehat{d}_n, \widehat{v}_n]^T$, $\boldsymbol{\omega}_n = [\omega_\phi, \omega_d, \omega_v]^T$ and $\mathbf{z}_n = [z_\phi, z_d, z_v]^T$. As considered above, both $\boldsymbol{\omega}_n$ and $\mathbf{z}_n$ are of covariance matrices being expressed as

$$\mathbf{Q}_w = \text{diag}\left(\bar{\sigma}_\phi^2, \bar{\sigma}_d^2, \bar{\sigma}_v^2\right), \ \mathbf{Q}_z = \text{diag}\left(\sigma_\phi^2, \sigma_d^2, \sigma_v^2\right). \quad (26)$$

Because of the non-linearity of the state evolution model, the standard Kalman filtering can not be directly utilized.

Algorithm 1: Predictive beam tracking of ISAC-DB.

1: **Step 1)** State prediction: $\widehat{\mathbf{x}}_{n|n-1} = \mathbf{h}\left(\widehat{\mathbf{x}}_{n-1}\right).$
2: **Step 2)** Linearization: $\mathbf{H}_{n-1} = \frac{\partial \mathbf{h}}{\partial \mathbf{x}}\bigg|_{\mathbf{x}=\widehat{\mathbf{x}}_{n-1}}.$
3: **Step 3)** Mean square error (MSE) matrix prediction: $\mathbf{M}_{n|n-1} = \mathbf{H}_{n-1} \mathbf{M}_{n-1} \mathbf{H}_{n-1}^H + \mathbf{Q}_\omega.$
4: **Step 4)** Kalman gain calculation: $\mathbf{K}_n = \mathbf{M}_{n|n-1} \left(\mathbf{M}_{n|n-1} + \mathbf{Q}_z\right)^{-1}.$
5: Transmit antenna number update with (22).
6: Measurement update: $\mathbf{y}_n = \mathbf{x}_n + \mathbf{z}_n.$
7: **Step 5)** State tracking: $\widehat{\mathbf{x}}_n = \widehat{\mathbf{x}}_{n|n-1} + \mathbf{K}_n \left(\mathbf{y}_n - \widehat{\mathbf{x}}_{n|n-1}\right).$
8: **Step 6)** MSE matrix update: $\mathbf{M}_n = \left(\mathbf{I}_3 - \mathbf{K}_n\right) \mathbf{M}_{n|n-1}.$
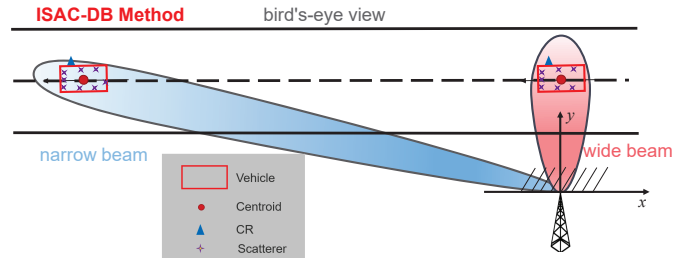

Fig. 4. Scenario of ISAC-DB: a benchmark design with the dynamic beamwidth for beam tracking.
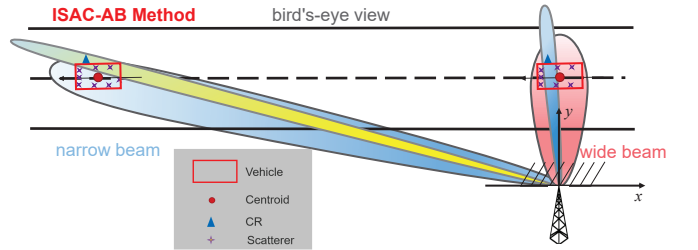

Fig. 5. Scenario of ISAC-AB: a more advanced design with alternant wide beam and narrow beam for beam tracking.

Therefore, EKF is used by linearizing the state evolution model, where the Jacobian matrix should be derived as

$$\mathbf{H} = \frac{\partial \mathbf{h}}{\partial \mathbf{x}} = \begin{bmatrix} 1 + \frac{v\Delta T \cos(\phi)}{d} & -\frac{v\Delta T \sin(\phi)}{d^2} & 0 \\ v\Delta T \sin(\phi) & 1 & -\Delta T \cos(\phi) \\ 0 & 0 & 1 \end{bmatrix}. \quad (27)$$

Before presenting the EKF technique, the remaining problem is the initialization of algorithm. In practice, it can be achieved with a conventional beam training with limited pilots at the beginning of the frame structure, then $\widehat{\phi}_0$, $\widehat{d}_0$ and $\widehat{v}_0$ can be generated. Following the standard procedure of EKF [29] with **Step 1)-6)**, the state prediction and tracking are summarized in Algorithm 1.

B. ISAC-AB Method

ISAC-DB requires the entire coverage of the vehicle with a dynamic wide beam, so that the position of the CR can be inferred relying on the resolved extended target profile. However, when the vehicle approaches the RSU, the wider

This article has been accepted for publication in IEEE Transactions on Wireless Communications. This is the author's version which has not been fully edited and content may change prior to final publication. Citation information: DOI 10.1109/TWC.2022.3219890
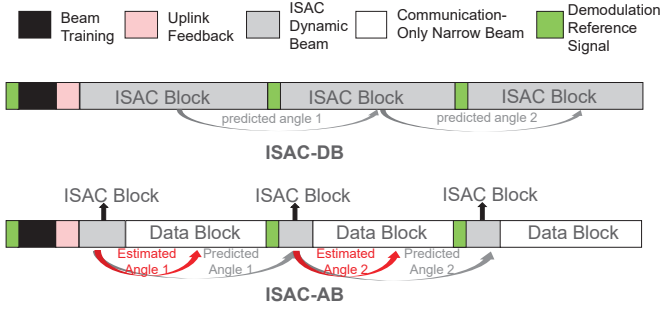
7

Fig. 6. Frame structures of the proposed schemes.

beam adopted deteriorates the communication performance due to the lower array gain. To balance such a contradiction, we further design a more advanced scheme wherein each block is divided into two parts: the former part transmits a wide beam for ISAC transmission, while the latter part is solely for communication by using a narrow beam which aligns the CR with the angle estimated from the former part. This is because the narrow beam is incapable of covering the entire vehicle geometry, thus the position of the CR can not be inferred according to the resolved geometry information. A scheme diagram is illustrated in Fig. 5. Besides, we also refer readers to Fig. 6 for more distinct expressions of the frame structures.

Denote the achievable rates of the wide beam and the narrow beam by R_n^{wide} and R_n^{narrow}, respectively. We introduce a time splitting factor as ρ, then the goal we wish to achieve is to maximize the average achievable rate in each block. Since only the former part in each block is used for sensing, ρ has a similar interpretation to the concept of duty ratio in each pulse repetition interval (PRI) [21]. To elaborate, in the nth epoch, the optimization model is formulated as

$$\rho_{\text{opt}} = \arg\max_{\rho} \ \rho R_n^{\text{wide}} + (1-\rho)R_n^{\text{narrow}}$$
$$s.t. \ 0 < \rho \leq 1. \tag{28}$$

Interpretation of the tradeoff relationship: When beams are aligned, it is apparent that $R_n^{\text{narrow}} \gg R_n^{\text{wide}}$ due to the much higher array gain of narrow beam, so that one aims to make ρ as small as possible, i.e., to allocate longer time duration to the narrow beam. However, an excessively small ρ may result in a failed tracking, which yields beam misalignment. In this case, the second term of the objective function becomes zero[7]. However, the CR can not be outside the wide beam such that $R_n^{\text{wide}} > 0$ always holds. Inherently, there is a noteworthy tradeoff relationship in such an interesting problem. The remaining task is to find the optimum solution of ρ.

Now, denote the beam alignment probability for the narrow beam by P_A. Then the average achievable rate is formulated as

$$R_n^{\text{narrow}} = \int_{\Omega} R p(R) dR \approx P_A R_{\text{align},n}^{\text{narrow}} + (1-P_A)R_{\text{mis},n}^{\text{narrow}},$$
$$\tag{29}$$

[7]In fact, beam sidelobes towards the CR still have an impact on the communication performance. However, the resulting achievable rate is small enough and can be approximately ignored.

where $R \in \Omega \triangleq R_{\text{align},n}^{\text{narrow}} \cup R_{\text{mis},n}^{\text{narrow}}$, and $R_{\text{align},n}^{\text{narrow}}$ and $R_{\text{mis},n}^{\text{narrow}}$ represent the achievable rates of beam alignment and beam misalignment for the narrow beam, respectively.

To summarize, R_n^{wide}, $R_{\text{align},n}^{\text{narrow}}$ and $R_{\text{mis},n}^{\text{narrow}}$ are expressed as

$$R_n^{\text{wide}} = \log\left(1 + p_n \frac{|\alpha_n \kappa_n^C \mathbf{a}_n^H(\phi_n)\mathbf{a}_n(\widehat{\phi}_{n|n-1})|^2}{\sigma_c^2}\right), \tag{30}$$

$$R_{\text{align},n}^{\text{narrow}} = \log\left(1 + p_n \frac{|\alpha_n \bar{\kappa}^C \bar{\mathbf{a}}^H(\phi_n)\bar{\mathbf{a}}(\widehat{\phi}_n)|^2}{\sigma_c^2}\right), \tag{31}$$

$$R_{\text{mis},n}^{\text{narrow}} = 0, \tag{32}$$

where the beamforming vector $\mathbf{f}_n^{\text{narrow}}$ for the narrow beam is used in (31), which is designed by exploiting the estimated results, given as

$$\mathbf{f}_n^{\text{narrow}} = \bar{\mathbf{a}}\left(\widehat{\phi}_n\right). \tag{33}$$

Note that $\bar{\kappa}^C$ and $\bar{\mathbf{a}}(\phi)$ are totally different from κ_n^C and $\mathbf{a}(\phi)$. For $\bar{\kappa}^C$ and $\bar{\mathbf{a}}(\phi)$, they are fixed with a constant number of mMIMO antennas. Here, we have

$$\bar{\mathbf{a}}(\phi) = \frac{1}{\sqrt{N_t^{\text{narrow}}}}\left[1, e^{-j\pi\cos\phi}, \cdots, e^{-j\pi(N_t^{\text{narrow}}-1)\cos\phi}\right]^T,$$
$$\tag{34}$$

and

$$\bar{\kappa}^C = \sqrt{N_t^{\text{narrow}}}, \tag{35}$$

where N_t^{narrow} denotes the antenna number of the narrow beam and is constant according to the system configuration. Thus, $\bar{\kappa}^C$ has no subscript. As for κ_n^C and $\mathbf{a}_n(\phi)$, they are dynamic because the beamwidth of the wide beam varies to cover the entire vehicle geometry. Both the predicted angle from the last epoch (i.e., $\widehat{\phi}_{n|n-1}$) and the estimated angle from the current epoch (i.e., $\widehat{\phi}_n$) are combined in the objective function. It is highlighted that $\widehat{\phi}_{n|n-1}$ is irrelevant to the current ρ at the nth epoch, while $\widehat{\phi}_n$ is relevant.

Substituting (29), (30), (31) and (32) into (28) yields

$$\rho_{\text{opt}} = \arg\max_{\rho} \ \rho \log\left(1 + p_n \frac{|\alpha_n \kappa_n^C \mathbf{a}_n^H(\phi_n)\mathbf{a}_n(\widehat{\phi}_{n|n-1})|^2}{\sigma_c^2}\right)$$
$$+ (1-\rho)P_A \log\left(1 + p_n \frac{|\alpha_n \bar{\kappa}^C \bar{\mathbf{a}}^H(\phi_n)\bar{\mathbf{a}}(\widehat{\phi}_n)|^2}{\sigma_c^2}\right)$$
$$s.t. \ 0 < \rho \leq 1.$$
$$\tag{36}$$

To proceed, it is assumed that $\widehat{\phi}_n$ follows a Gaussian distribution around the true angle ϕ_n as $\widehat{\phi}_n \sim \mathcal{N}(\phi_n, \lambda_n^2)$. In ISAC-AB, the matched-filtering gain of the wide beam in the first part decreases by ρG times since the matched-filtering gain equals to the number of symbols in a block [16]. If we let σ_ϕ^2 represent the angle variance when $\rho = 1$ as discussed before in Sec. III-A, then $\lambda_n^2 = \sigma_\phi^2/\rho$. The narrow beam is aligned only if the estimated angle in the wide beam satisfies $\left|\widehat{\phi}_n - \phi_n\right| < \delta_n$, where δ_n denotes the half-beamwidth of narrow beam defined in (20), i.e.,

$$\delta_n = \frac{0.89}{N_t^{\text{narrow}}\sin(\widehat{\phi}_n)}. \tag{37}$$

However, the dependence of δ_n on $\widehat{\phi}_n$ is not beneficial to the following derivations. Specifically, the estimation accuracy of $\widehat{\phi}_n$ is affected by the current ρ_{opt} while we hope to obtain ρ_{opt} according to the known $\widehat{\phi}_n$. To proceed, we use the predicted $\widehat{\phi}_{n|n-1}$ instead because its prediction accuracy is determined by the last ρ and is irrelevant to the current ρ. In brief, in the optimization model we now use

$$\delta_n \approx \frac{0.89}{N_t^{\text{narrow}} \sin(\widehat{\phi}_{n|n-1})}. \tag{38}$$

Likewise, despite the true value of α_n being $\alpha_n = \alpha_{\text{ref}} d_n^{-1} e^{j \frac{2\pi f_c}{c} d_n}$ which is unknown in practice, we use $\widehat{\alpha}_{n|n-1} = \alpha_{\text{ref}} \widehat{d}_{n|n-1}^{-1} e^{j \frac{2\pi f_c}{c} \widehat{d}_{n|n-1}}$ in the optimization for the same reason, for both the wide beam and the narrow beam.

Now, the task left is to derive the beam alignment probability of the narrow beam, which is given as

$$
\begin{aligned}
P_A &= \Pr\left\{\widehat{\phi}_n \le \phi_n + \delta_n\right\} - \Pr\left\{\widehat{\phi}_n \le \phi_n - \delta_n\right\} \\
&= \frac{1}{2}\left(1 + \text{erf}\left(\frac{\delta_n}{\sqrt{2}\lambda_n}\right)\right) - \frac{1}{2}\left(1 + \text{erf}\left(\frac{-\delta_n}{\sqrt{2}\lambda_n}\right)\right) \\
&= \text{erf}\left(\frac{\delta_n}{\sqrt{2}\lambda_n}\right),
\end{aligned}
\tag{39}
$$

where $\text{erf}(\cdot)$ represents the error function and $\Pr(X \le x) = \int_{-\infty}^{x} p_X(y)dy$. Accordingly, the optimization problem is further recast as

$$
\rho_{\text{opt}} = \arg\max_{\rho} \; \rho \log\left(1 + p_n \frac{|\widehat{\alpha}_{n|n-1}\kappa_n^C \mathbf{a}_n^H(\phi_n)\mathbf{a}_n(\widehat{\phi}_{n|n-1})|^2}{\sigma_c^2}\right)
$$
$$
+ (1-\rho)\text{erf}\left(\sqrt{\frac{\rho}{2}}\frac{\delta_n}{\sigma_\phi}\right)\log\left(1 + p_n \frac{|\widehat{\alpha}_{n|n-1}\bar{\kappa}^C \bar{\mathbf{a}}^H(\phi_n)\bar{\mathbf{a}}(\widehat{\phi}_n)|^2}{\sigma_c^2}\right)
$$
$$
s.t. \; 0 < \rho \le 1.
\tag{40}
$$

Unfortunately, it is still impossible to obtain ϕ_n and $\widehat{\phi}_n$ ahead of the signaling transmission at the nth epoch. Firstly, the true angle ϕ_n is always unknown for the RSU. Moreover, the estimated angle $\widehat{\phi}_n$ is neither known a priori. In fact, it is not until (40) is solved that we can devise the block splitting scheme and transmit the first wide-beam part, and subsequently acquire $\widehat{\phi}_n$. To tackle this apparent contradiction and for a practical application, $\left|\mathbf{a}_n^H(\phi_n)\mathbf{a}_n(\widehat{\phi}_{n|n-1})\right| = \left|\frac{\sin(\pi N_{t,n}(\cos\phi_n - \cos\widehat{\phi}_{n|n-1}))}{N_{t,n}\sin(\pi(\cos\phi_n - \cos\widehat{\phi}_{n|n-1}))}\right|^2 = 1$ [8] and $\left|\bar{\mathbf{a}}^H(\phi_n)\bar{\mathbf{a}}(\widehat{\phi}_n)\right| = \left|\frac{\sin(\pi N_t^{\text{narrow}}(\cos\phi_n - \cos\widehat{\phi}_n))}{N_t^{\text{narrow}}\sin(\pi(\cos\phi_n - \cos\widehat{\phi}_n))}\right|^2 = 1$ can be exploited by assuming that perfect beam alignments (PBA) are reached, leading to a *suboptimum* solution. Finally, the considered model is

---

[8]The first part with the wide beam can always cover the entire vehicle. Moreover, it contributes much less percent in the average achievable rate, so that we can use $|\mathbf{a}_n^H(\phi_n)\mathbf{a}_n(\widehat{\phi}_{n|n-1})|^2 = 1$ in the optimization problem for simplifications.
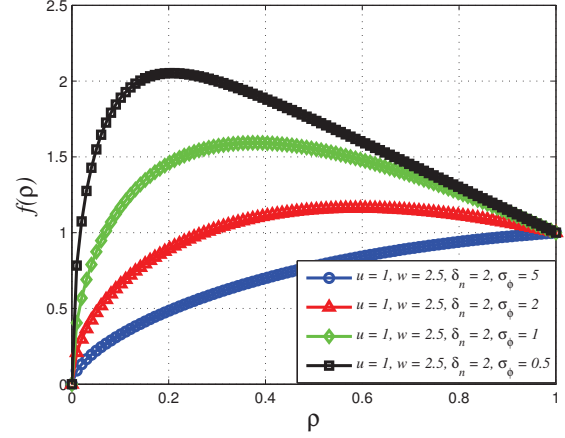

Fig. 7. The objective function in (41) $f(\rho)$ versus ρ.

simplified as

$$
\rho_{\text{opt}} = \arg\max_{\rho} \; \rho \log\left(1 + p_n \frac{|\widehat{\alpha}_{n|n-1}\kappa_n^C|^2}{\sigma_c^2}\right)
$$
$$
+ (1-\rho)\text{erf}\left(\sqrt{\frac{\rho}{2}}\frac{\delta_n}{\sigma_\phi}\right)\log\left(1 + p_n \frac{|\widehat{\alpha}_{n|n-1}\bar{\kappa}^C|^2}{\sigma_c^2}\right)
$$
$$
s.t. \; 0 < \rho \le 1.
\tag{41}
$$

Theorem: The model (41) is a convex optimization problem.

Proof: To elaborate, we denote $u \triangleq \log\left(1 + p_n \frac{|\alpha_n \kappa_n^C|^2}{\sigma_c^2}\right) > 0$, $v \triangleq \frac{\delta_n}{\sqrt{2}\sigma_\phi} > 0$, and $w \triangleq \log\left(1 + p_n \frac{|\alpha_n \bar{\kappa}^C|^2}{\sigma_c^2}\right) > 0$. Here, u, v and w are independent of ρ. Denote the objective function in (41) by $f(\rho)$. Then the first-order derivative with respect to ρ is derived as

$$f'(\rho) = u + \frac{wv}{\sqrt{\pi}}(\rho^{-\frac{1}{2}} - \rho^{\frac{1}{2}})e^{-\rho v^2} - w\,\text{erf}(\sqrt{\rho}v). \tag{42}$$

Therefore, the second-order derivative is further derived as

$$f''(\rho) = -\frac{wv}{\sqrt{\pi}}e^{-v^2\rho}\left(\frac{3}{2}\rho^{-\frac{1}{2}} + \frac{1}{2}\rho^{-\frac{3}{2}} + v^2\rho^{-\frac{1}{2}} - v^2\rho^{\frac{1}{2}}\right) < 0, \tag{43}$$

where $\partial\text{erf}(x)/\partial x = 2/\sqrt{\pi}e^{-x^2}$ and $0 < \rho \le 1$ are used. The proof is thus completed in terms of the negative second-order derivative and the linear feasible set. To vividly illustrate the convexity of (41), numerical curves of $f(\rho)$ for $0 < \rho \le 1$ are provided in Fig. 7. Obviously, all curves are concave while the optimization is to find the maximum value. Hence, the convexity of (41) is verified. Additionally, ρ_{opt} is enlarged with the increasing σ_ϕ^2, which indicates that more time durations for the wide beam is needed to ensure the beam alignment for the narrow beam in the low-SNR regime.

To solve problem (41), let us define its Lagrangian multiplier as

$$\mathcal{L}(\rho, \eta, \varsigma) = -f(\rho) - \eta\rho + \varsigma(\rho - 1), \tag{44}$$

where $\eta \geq 0$ and $\varsigma \geq 0$. According to [38], the Karush-Kuhn-Tucker (KKT) condition of (41) is derived as

$$\begin{cases} \mathcal{L}'(\rho_{\text{opt}}, \eta^*, \varsigma^*) = -f'(\rho_{\text{opt}}) - \eta^* + \varsigma^* = 0, \\ \eta^* \geq 0, \ \varsigma^* \geq 0, \ \eta^* \rho_{\text{opt}} = 0, \ \varsigma^*(\rho_{\text{opt}} - 1) = 0, \ 0 < \rho_{\text{opt}} \leq 1. \end{cases}$$
(45)

It is readily to see that the optimum solution is calculated as $\rho_{\text{opt}} = \begin{cases} 1 & f'(1) \geq 0 \\ \rho^* & \text{otherwise} \end{cases}$, where ρ^* is the sole root of $f'(\rho^*) = 0$, which can be achieved by a trivial grid search.

Finally, the detailed steps of ISAC-AB can be summarized in Algorithm 2.

Algorithm 2: Predictive beam tracking of ISAC-AB.

1: **for** $n = 1, 2, \cdots$ **do**
2:   At the nth epoch, solve (41) to obtain ρ_{opt}.
3:   Beam tracking with the wide beam in $t \in [n\Delta T, (n + \rho_{\text{opt}})\Delta T)$: Following the steps in Algorithm 1, where the beamforming vector is designed with the predicted angle from the last epoch as $\mathbf{f}_n = \mathbf{a}_n \left(\widehat{\phi}_{n|n-1} \right)$.
4:   Communicating with the narrow beam in $t \in [(n + \rho_{\text{opt}})\Delta T, (n + 1)\Delta T)$: The beamforming vector is designed with the estimated angle from the current epoch as $\bar{\mathbf{f}}_n = \bar{\mathbf{a}} \left(\widehat{\phi}_n \right)$.
5: **end for**

We highlight that (41) is a relaxation of the original problem and therefore its solution is suboptimal. By solving (41), ρ_{opt} is obtained and thus the real achievable rate at the nth epoch is given as

$$\begin{aligned} R_n^{\text{opt}} = &\rho_{\text{opt}} \log \left(1 + p_n \frac{|\alpha_n \kappa_n^C \mathbf{a}_n^H(\phi_n) \mathbf{a}_n(\widehat{\phi}_{n|n-1})|^2}{\sigma_c^2} \right) \\ &+ (1 - \rho_{\text{opt}}) \log \left(1 + p_n \frac{|\alpha_n \bar{\kappa}^C \bar{\mathbf{a}}^H(\phi_n) \bar{\mathbf{a}}(\widehat{\phi}_n)|^2}{\sigma_c^2} \right). \end{aligned}$$
(46)

For comparison in subsequent simulations, the value of optimal objective function of (41) at the nth epoch is also given as

$$\begin{aligned} R_n^{\text{obj,opt}} = &\rho_{\text{opt}} \log \left(1 + p_n \frac{|\widehat{\alpha}_{n|n-1} \kappa_n^C|^2}{\sigma_c^2} \right) \\ &+ (1 - \rho_{\text{opt}}) \text{erf} \left(\sqrt{\frac{\rho_{\text{opt}}}{2}} \frac{\delta_n}{\sigma_\phi} \right) \log \left(1 + p_n \frac{|\widehat{\alpha}_{n|n-1} \bar{\kappa}^C|^2}{\sigma_c^2} \right). \end{aligned}$$
(47)

Note that $R_n^{\text{obj,opt}}$ is actually the approximately optimal average achievable rate since the effects of $|\mathbf{a}_n^H(\phi_n) \mathbf{a}_n(\widehat{\phi}_{n|n-1})|^2$ and $|\bar{\mathbf{a}}^H(\phi_n) \bar{\mathbf{a}}(\widehat{\phi}_n)|^2$ are ignored in (47). Therefore, $R_n^{\text{obj,opt}}$ can not represent the real achievable rate in terms of the deliberate idealization of the beamforming gain. Moreover, there would be a rate gap between $R_n^{\text{obj,opt}}$ and R_n^{opt}, especially when measurement variances are relatively large. A special case of $R_n^{\text{obj,opt}} \approx R_n^{\text{opt}}$ holds when measurement variances are small enough (or equivalently, SNR is infinitely high), in which both the wide beam and the narrow beam are accurately

aligned, i.e., $|\mathbf{a}_n^H(\phi_n) \mathbf{a}_n(\widehat{\phi}_{n|n-1})|^2 \approx 1$, $|\bar{\mathbf{a}}^H(\phi_n) \bar{\mathbf{a}}(\widehat{\phi}_n)|^2 \approx 1$ and $P_A \approx 1$.

Remark 2: In this article, the beam alignment makes sense in the half-power beamwidth of beampattern, which indicates that $\frac{1}{2} \leq |\bar{\mathbf{a}}^H(\phi_n) \bar{\mathbf{a}}(\widehat{\phi}_n)|^2 \leq 1$. In addition to the case of PBA, intuitively, the case of worst beam alignment (WBA) (i.e. $|\bar{\mathbf{a}}^H(\phi_n) \bar{\mathbf{a}}(\widehat{\phi}_n)|^2 = \frac{1}{2}$) can also be a candidate for the optimization. However, numerical results in subsequent simulations demonstrate that true achievable rates of PBA and WBA are nearly identical. Given this reason, we only take PBA as an example in the rest of simulations, if not specifically mentioned.

Finally, a brief complexity analysis of ISAC-DB and ISAC-AB is given. For the steps of EKF in Algorithm 1, there are 4 matrix multiplications and 1 matrix inversion. On account of the 3×1 dimensional state vector, the total complexity for ISAC-DB in $T/\Delta T$ data blocks is $135T/\Delta T$. As for ISAC-AB, an additional complexity $UT/\Delta T$ is generated due to the grid search in solving (41), where U denotes the number of grid bins.

TABLE I
PARAMETERS IN SIMULATIONS.

Parameter	Value	Parameter	Value
T	$8.0s$	ΔT	$0.01s$
f_c	30GHz	p_n	1
Δd	$6m$	v	$20m/s$
Δx	$1.5m$	Δy	$0.5m$
N_t^{narrow}	128	$N_{t,\max}$	128
a_1	$1.05e^{-2}$	a_2	$3.5e^{-2}$
a_3	$1.05e^{-2}$	N_r	128
K	8	$\bar{\sigma}_\phi$	$0.01°$
$\bar{\sigma}_d$	$0.1m$	$\bar{\sigma}_v$	$0.25m/s$
σ^2	0.15	σ_C^2	1
G	10	α_{ref}	1

IV. SIMULATIONS

In this section, we provide numerical simulation results to verify the proposed V2I beam tracking schemes. If not otherwise specified, the simulative parameters follows Table. I. Beyond that, we assume that the coordinate of RSU is $(0m, 0m)$, and the initial position of the vehicle in the interested region is $(60m, 20m)$. In simulations, we model the vehicle with resolved scatterers uniformly distributed in the spatial geometry shape. The RCS of slowly fluctuated scatterers $\varepsilon_{k,n}$ are generated by a complex Gaussian distribution with zero mean and unit variance. Besides, the vehicle moves in the direction of the negative x-axis. All results are averaged by 500 runs.

A. Performance Evaluation of ISAC-DB Method

The achievable rates of ISAC-DB with known variances and approximated variances are provided in Fig. 8(a) with different transmit SNR defined as $\frac{p_n}{\sigma^2}$. Three transmit SNR values are SNR = 5.23dB ($p_n = 0.5, \sigma^2 = 0.15$), SNR = 8.24dB
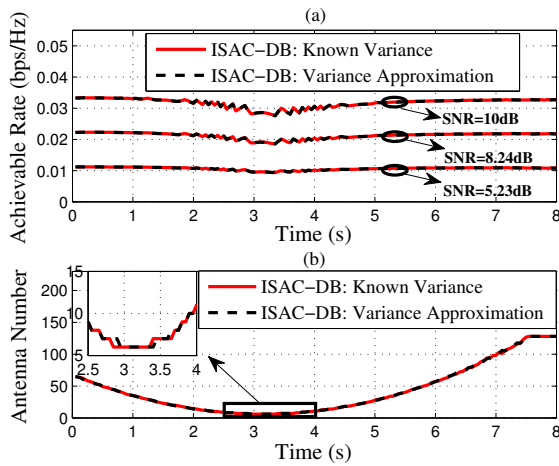
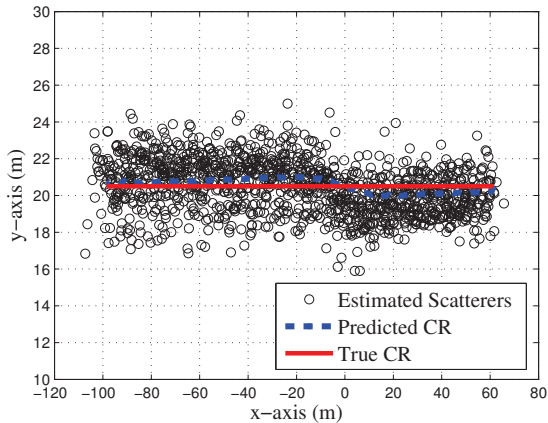Fig. 8. (a) Achievable rate versus time; (b) $N_{t,n}$ versus time.

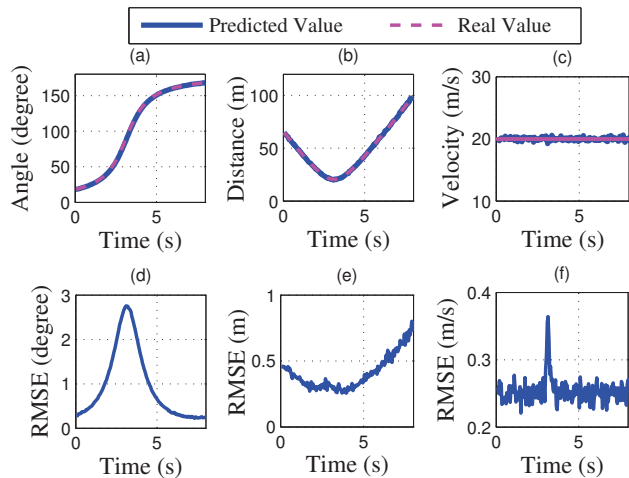Fig. 9. Trajectory tracking in a 2D plane.

Fig. 10. Performances of ISAC-DB. (a) Predicted angle and real angle; (b) Predicted distance and real distance; (c) Predicted velocity and real velocity; (d) RMSE of predicted angle; (e) RMSE of predicted distance; (f) RMSE of predicted velocity.

limitation of system configuration at this moment.

Trajectory tracking results in a 2D plane with ISAC-DB are provided in Fig. 9, which include trajectories of the predicted CR and the real CR, together with the resolved scatterers at each time instant. In general, the two trajectories coincide well. When the vehicle approaches the RSU, the prediction error increases due to the decline of array gain and thereby the trajectory gap becomes relatively larger. Accordingly, predicted values and real values of angle, distance and velocity are shown in Fig. 10. To evaluate the prediction accuracy, the root mean square error (RMSE) curves of angle, distance and velocity are also illustrated in Fig. 10. It is found that the RMSE of angle increases when the vehicle approaches the RSU, in terms of the large angular variation. As for the RMSE of distance, there is no such a phenomenon because the distance variation is small at this moment. Besides, there is a peak in the RMSE of velocity, on account of the sufficiently small radial velocity measured when the RSU is approaching, leading to a relatively large prediction error. Overall, the prediction procedure exhibits a high accuracy.

B. Performance Evaluation of ISAC-AB Method

Now, we concentrate on the communication performance of the advanced ISAC-AB method with known variances in Fig. 11 and approximated variances in Fig. 12. By solving (41), ρ_{opt} is obtained in Fig. 11(a) and Fig. 12(a), respectively. As shown in the enlarged images, ρ_{opt} in Fig. 12(a) has the similar trend to that in Fig. 11(a). It is noticed that the values of ρ_{opt} are relatively small in the region of $t \in [0, 7]s$, on account of the parameter setting in the simulations. If the noise power is larger or the transmit power is smaller, then it is expected that the system allocates the longer time duration for the dynamic beam in the first part. It is also noticed that PBA and WBA result in almost equal ρ_{opt} in both figures. When the vehicle approaches the RSU, the dynamic beam is with smaller array gain. Thus, to guarantee the prediction

$(p_n = 1, \sigma^2 = 0.15)$ and SNR = 10dB $(p_n = 1.5, \sigma^2 = 0.15)$, respectively. Here, key findings emerge: 1) The achievable rate increases with the larger transmit SNR; 2) Approximated variances have a tiny effect in communication performance of ISAC-DB relative to the real variances, which verifies the effectiveness of variance approximations; 3) The achievable rate R_n deteriorates when the vehicle approaches the RSU, which indicates that the receive SNR (i.e., SNR_n^C defined in (19)) reduces. For the fixed beamwidth and the transmit signal power in [16], it is foreseen that R_n increases when the vehicle approaches the RSU due to the stronger LoS channel coefficient corresponding to the higher SNR_n^C. We also provide the numerical result of $N_{t,n}$ in Fig. 8(b) when SNR = 8.24dB with known variance and approximated variance, respectively. Interestingly, when the vehicle approaches the RSU, $N_{t,n}$ decreases for covering the entire vehicle and ISAC-DB thus achieves the lower achievable rate, which is different from the results in [16]. This indicates that the power attenuation caused by the smaller $N_{t,n}$ plays a more dominated role than the approaching range in affecting SNR_n^C. In addition, when the vehicle drives away near to $t = 8s$, the antenna number calculated by (22) is fixed at $N_{t,\max} = 128$, which attains the
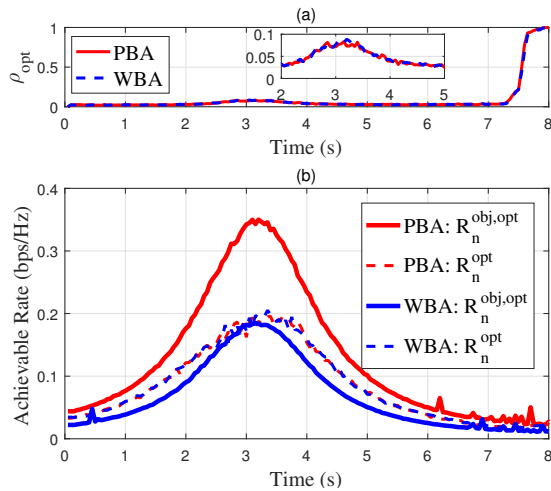
Fig. 11. ISAC-AB with known variances. (a) ρ_{opt} with PBA and WBA, respectively; (b) Optimized objective functions $R_n^{\text{obj,opt}}$ with PBA and WBA, and true achievable rates R_n^{opt} with PBA and WBA, respectively.

Fig. 13. True angle variance and approximated counterpart with the first-order Taylor expansion. (a) Variance versus time; (b) PDF versus angle at $t = 1s$; (c) PDF versus angle at $t = 3s$; (d) PDF versus angle at $t = 7s$.
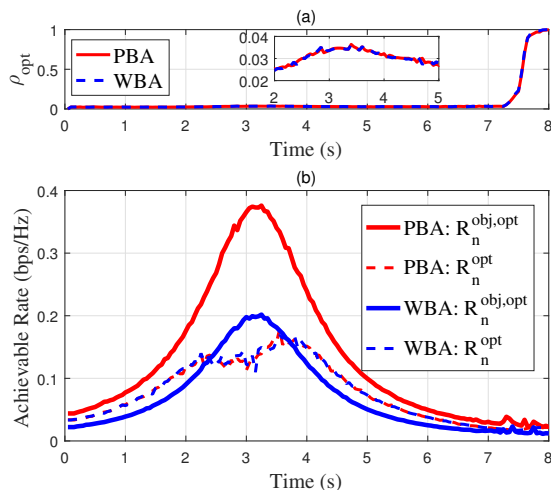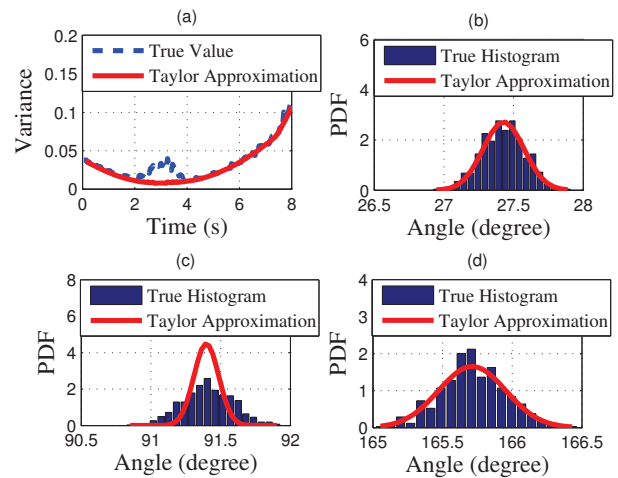

Fig. 12. ISAC-AB with approximated variances. (a) ρ_{opt} with PBA and WBA, respectively; (b) Optimized objective functions $R_n^{\text{obj,opt}}$ with PBA and WBA, and true achievable rates R_n^{opt} with PBA and WBA, respectively.
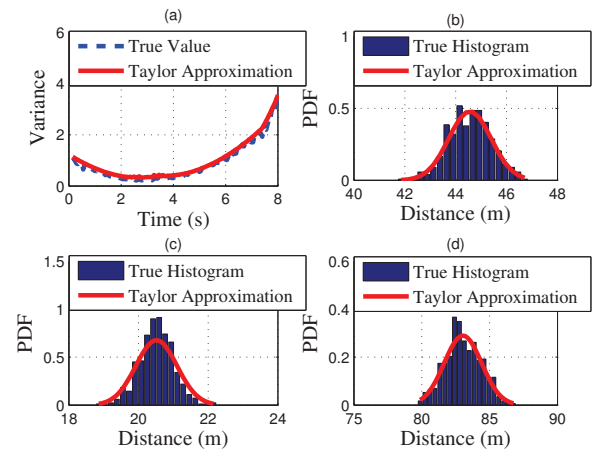

Fig. 14. True distance variance and approximated counterpart with the first-order Taylor expansion. (a) Variance versus time; (b) PDF versus angle at $t = 1s$; (c) PDF versus angle at $t = 3s$; (d) PDF versus angle at $t = 7s$.

accuracy, the optimization allocates longer duration for the first part to achieve higher matched-filtering gain. It is also demonstrated that $\rho_{\text{opt}} \approx 1$ in the near region of the epoch $t = 8s$. This is because when the vehicle drives away, the antenna number calculated by (22) is fixed at $N_{t,\max} = 128$. Then the first part and the second part of ISAC-AB are with the same antenna number. Hence, $\rho_{\text{opt}} = 1$ is attained and the matched-filtering gain can not be added anymore, so that the beam tracking performance gradually deteriorates. That is why small fluctuations appear nearby the region of $t = 8s$.

As stated above, the achievable rate of ISAC-DB degrades when approaching the RSU due to the loss of array gain. In Fig. 11(b) and Fig. 12(b), however, ISAC-AB is able to perfectly overcome such a dilemma since its rate is principally contributed by the second part with a narrow beam of the high array gain. Hence, when the vehicle is approaching, the achievable rate improves in terms of the shorter distance and

the fixed array gain.

Besides, we also provide the comparison among four cases with ISAC-AB in Fig. 11(b) and Fig. 12(b), respectively. Firstly, we consider the case in which the variances of σ_ϕ^2, σ_d^2 and σ_v^2 are known. In Fig. 11(b), the true achievable rate R_n^{opt} of PBA calculated by (46) has a certain gap to the optimized objective function $R_n^{\text{obj,opt}}$ of PBA calculated by (47). In fact, $R_n^{\text{obj,opt}}$ of PBA can not represent the real achievable rate in terms of the deliberate idealization of the beamforming gain. In other words, the approximations always assume PBA, which is unreal for EKF in the noisy environment. A special case occurs when measurement variances are small enough, so that the predicted $\widehat{\phi}_{n|n-1}$ and the estimated $\widehat{\phi}_n$ equal to the true ϕ_n, and the P_A of the narrow beam equals to 1. In that way, (46) and (47) are equivalent. In contrast, when WBA is utilized, $R_n^{\text{obj,opt}}$ is lower than R_n^{opt}. Note that $R_n^{\text{obj,opt}}$ of WBA denotes the optimized objective function of WBA, which has a similar form as (47) of PBA, except that $|\bar{\mathbf{a}}^H(\phi_n)\bar{\mathbf{a}}(\widehat{\phi}_n)|^2 = \frac{1}{2}$ is used.

Now, we consider the case in which the variances of σ_ϕ^2, σ_d^2 and σ_v^2 are unknown, and validate the availability of the developed variance approximations. It is found that the approximation accuracy of σ_v^2 has a tiny effect on the beam tracking in simulations. Here, regardless of the approximated σ_v^2 obtained by (61), we only investigate the the feasibility of the first-order Taylor expansions on σ_ϕ^2 and σ_d^2. Note that the true variances of angle and distance at the nth epoch are calculated as $\sigma_\phi^2 = E[(\widehat{\phi}_n - \phi_n)^2]$ and $\sigma_d^2 = E[(\widehat{d}_n - d_n)^2]$. In Fig. 13(a), the true variance σ_ϕ^2 becomes smaller when the vehicle approaches the RSU, and raises when it drives away. However, at surroundings of the epoch $t = 3s$ corresponding to $\phi_n \approx \pi/2$, the angles of scatterers changes too fast in the high mobility scenarios, which causes the spikes for the estimation of ϕ_n. Meanwhile, it is found that the similar approximation of σ_d^2 in Fig. 14(a) performs better when $\phi_n \approx \pi/2$, since the distances of scatterers changes more slowly at this moment. Fortunately, the spikes of angle would not seriously affect the achievable rate, despite that some small fluctuations appear in the corresponding epoches. As shown by comparing Fig. 12(b) with Fig. 11(b), the true achievable rate with approximated variance has a slight performance loss relative to the case with known variance, which is caused by the approximation errors. Note however that the optimized objective functions with approximated variances exceed the optimized objective functions with true variances when $\phi_n \approx \pi/2$, since the approximated σ_ϕ^2 at this time is slightly smaller than the true value. Therefore, the smaller σ_ϕ^2 leads to the smaller ρ_{opt}, as shown by comparing Fig. 12(a) with Fig. 11(a). Moreover, in Fig. 12(b), it is shown that the true achievable rate of WBA would be smaller than the optimized objective function of WBA near to $\phi_n = \pi/2$. In this case, the smaller ρ_{opt} leads to a relatively coarse estimation of $\widehat{\phi}_n$ in the first part with the wide beam, and thus $|\bar{\mathbf{a}}^H(\phi_n)\bar{\mathbf{a}}(\widehat{\phi}_n)|^2 < \frac{1}{2}$ is attained in practice. Interestingly, it is observed that the true achievable rates of PBA and WBA are nearly equal in our numerical examples. For convenience, we only take the case of PBA as an example in the following, as its objective function provides a good insight of the idealistic behavior. However, it is worth mentioning that a real PBA could be attained only in the noise-free environment, or equivalently, when SNR is infinitely large.

Figs. 13(b)-(d) and Figs. 14(b)-(d) also provide the histograms of the measured $\widehat{\phi}_n$ and $\widehat{d}_n$ at epoches $t = 1s$, $t = 3s$ and $t = 7s$, respectively. Overall, the probability density functions (PDFs) of Gaussian fittings with approximated variances can well match the histograms. This again verifies that the feasibility of Gaussian assumptions and the effectiveness of variance approximations.

C. Performance Comparison Among the Proposed Schemes and State-of-The-Art Methods

We examine the superiorities of the proposed ISAC-DB and ISAC-AB by comparing with the following beam tracking algorithms:

- The auxiliary beam pair (ABP) algorithm, where a pair of training beams are transmitted within each block [24];
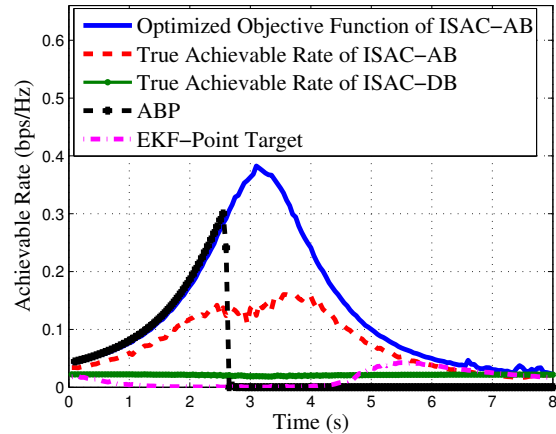
Fig. 15. Achievable rate comparison among different methods.
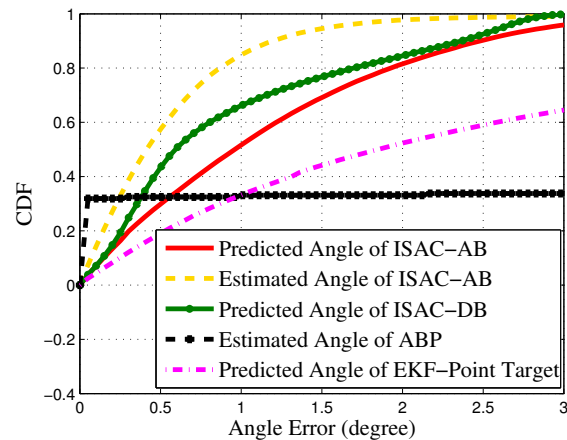

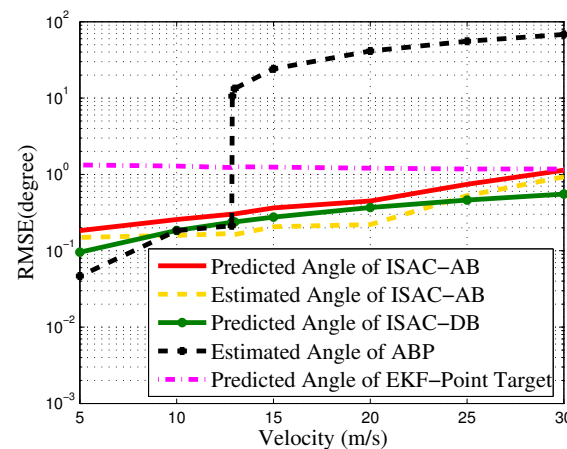Fig. 16. CDF comparison of overall angle tracking among ISAC-AB, ISAC-DB, ABP, and EKF-Point Target methods.

Fig. 17. RMSE comparison of overall angle versus velocity among ISAC-AB, ISAC-DB, ABP, and EKF-Point Target methods.

- EKF-based beam tracking algorithm for point target (denoted as " EKF-Point Target" in the following) [16].

Note that ABP algorithm belongs to the class of the

This article has been accepted for publication in IEEE Transactions on Wireless Communications. This is the author's version which has not been fully edited and content may change prior to final publication. Citation information: DOI 10.1109/TWC.2022.3219890

13

communication-only beam tracking which needs additional pilots of CSI-RS and uplink feedbacks, of which the overhead in front of each data block is much higher than the ISAC-based beam tracking. For the EKF-Point Target, as we highlight before, it is unable to precisely track the CR when the vehicle is extended in range and angle domains. For a fair comparison, we randomly select a scatterer of the vehicle (not in the position of CR) and track it. For the RSU, it treats this scatterer as the CR since the target is considered as point-like for EKF-Point Target. Note that both the two schemes are parameterized with a fixed number of transmit antennas as $N_t = 128$. For ABP, the half searching range of the beamforming region for the transmitter defined in [24] is set as $\frac{\pi}{32}$ without loss of generality.

The comparative results of these schemes are provided in Fig. 15. It is interesting to see that ISAC-AB achieves better performance than EKF-Point Target, while is inferior to ABP in the region of $t \in [0s, 2.6s]$. To account for this, we emphasize that ABP is a communication-only beam tracking algorithm with a fixed number of antennas as $N_t^{\text{narrow}} = 128$, corresponding to a narrow beam with the highest array gain. Hence, it surpasses ISAC-AB only if the tracking is successful, since the achievable rate of ISAC-AB is a combination of both the wide beam and the narrow beam. However, when the vehicle approaches the RSU, the angle changes faster, and the angular variation is sufficiently large which is not likely to fall into the searching range of the beamforming region as $\frac{\pi}{16}$. As such, the vehicle trajectory is lost and the beam tracking fails. As for the EKF-Point Target, it is much inferior to ISAC-AB due to the beam misalignment. In fact, when the vehicle approaches the RSU, the narrow beam with fixed $N_t = 128$ antennas is more unlikely to simultaneously cover both the tracked scatterer and CR, arising a drastic beam misalignment.

For the sake of a deeper perception, we further show the overall tracking performance via the cumulative distribution function (CDF) of angle prediction and/or estimation errors in Fig. 16. The results explicitly support the analysis above.

To show the superiority of the proposed methods in high-mobility scenarios, we firstly demonstrate the overall RMSE results of angle versus the velocity in Fig.17. The simulative velocities are set as $30m/s$, $25m/s$, $20m/s$, $15m/s$, $13m/s$, $12.875m/s$, $12.85m/s$, $10m/s$ and $5m/s$, respectively. The vehicle moves in the same trajectory of length $160m$. In general, ISAC-AB, ISAC-DB and ABP methods achieve worse RMSE tracking results with an increased velocity, because of a non-negligible movement in each epoch interval ΔT. For ISAC-AB and ISAC-DB methods, a lower velocity helps the CR to align the beam in ΔT. As for ABP, it is sensitive to the velocity. Especially when the velocity is larger than $12.875m/s$, ABP method rapidly breaks down since the angular variation is too large to fall into the searching range, which again verifies the superiority of ISAC-AB method over the conventional communication-only beam tracking methods in high mobility scenarios. Interestingly, EKF-Point Target method behaves slightly better with an increased velocity. Since it always tracks a selected scatterer, the CR may be closer to the narrow beam aligned to the scatterer, considering the movement in ΔT. Therefore, when the vehicle moves faster, the CR has a higher
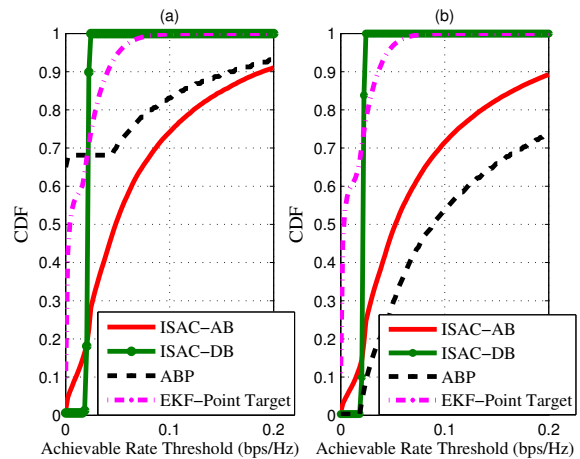

Fig. 18. CDF versus achievable rate threshold among ISAC-AB, ISAC-DB, ABP, and EKF-Point Target methods. (a) $v = 20m/s$; (b) $v = 10m/s$.
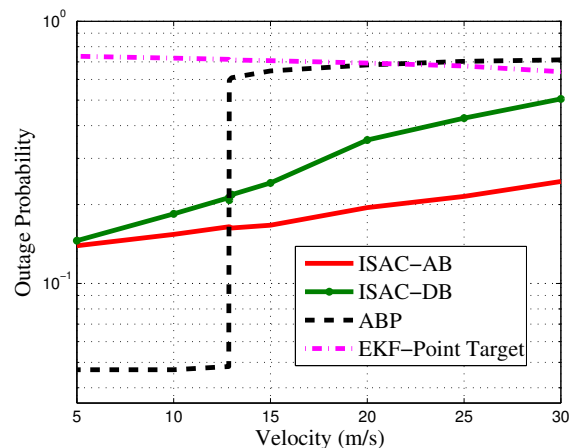

Fig. 19. Outage probability of overall achievable rate versus velocity among ISAC-AB, ISAC-DB, ABP, and EKF-Point Target methods.

probability to lie in the narrow beam if the scatterer is ahead of the CR in the direction of movement. In short, whether the performance of EKF-Point Target method can be improved with a larger velocity depends on the positions of CR, the tracked scatterer, and the direction of movement.

Next, we define the outage probability of overall achievable rate, which is given as

$$P_{\text{OUT}} = \frac{1}{T/\Delta T} \sum_{n=1}^{T/\Delta T} \Pr\{R_n \leq \gamma\}, \qquad (48)$$

where γ denotes the achievable rate threshold. In Fig. 18, we first demonstrate the CDF curves versus the achievable rate threshold, in cases of $v = 20m/s$ and $v = 10m/s$, respectively. Overall, when $v = 20m/s$, ISAC-AB method behaves better than ISAC-DB, ABP and EKF-Point Target methods in achieving higher rates. However, when $v = 10m/s$, ABP method outperforms other methods in general, benefiting from the low-mobility that the angular variation is small enough to fall into the searching range. In this case, ABP method is even superior to ISAC-AB method since the beam

is accurately aligned to the CR and the narrow beam with 128-antenna array is used in each entire block length ΔT.

For a further insight of the velocity impact, the outage probability curves versus different velocities are provided in Fig. 19, where the achievable rate threshold is set as $\gamma = 0.02$bps/Hz. For example, the mmWave signaling with a bandwidth as 500MHz is qualified to support the data transmission with 10Mbps data rate. It can be concluded that the proposed ISAC-AB and ISAC-DB methods, along with ABP method, achieve better communication transmission when the velocity is lower. Likewise, it is found that ABP method is sensitive to the velocity, as stated before. Overall, ISAC-AB method outperforms other methods in high-mobility scenarios, in terms of the outage probability performance.

V. Conclusion and Future Work

In this article, we have proposed novel schemes in regard to sensing-assisted mMIMO beam tracking for the extended target vehicle. Exploiting such an ISAC approach provides significant gains in terms of both sensing and communications. We have proposed EKF beam prediction approaches that exploit varying beamwidths. Our approaches, thanks to the extended target modeling, offer significant enhancements to state-of-the-art ISAC solutions by optimizing the beam tracking to focus on the CR. Finally, numerical results have verified the feasibility and the effectiveness of the proposed optimization scheme, which has remarkable superiorities over the state-of-the-art beam tracking approaches.

Future work will focus on the following aspects in V2I networks. First, beam tracking in the multi-target scenario, where the data association strategy should be specifically devised. Second, universal ISAC approaches in the arbitrary road trajectory, which needs an accurate road geometry modeling. Some preliminary results towards addressing this issue have been shown in [27]. Third, detailed evaluation and analysis on how much percent of overheads can be released in the 5G NR protocol, based on ISAC beam tracking.

Appendix
Approximations of measurement variances in (17)

Note that all $\widehat{\theta}_{k,n}$, $\widehat{d}_{k,n}$ and $\widehat{\mu}_{k,n}$ are Gaussian variables. However, due to the non-linearity of (17), $\widehat{\phi}_n$, $\widehat{d}_n$ and $\widehat{v}_n$ are not Gaussian, thus σ_ϕ^2, σ_d^2 and σ_v^2 are intractable. To resolve this problem, we resort to the first-order Taylor expansion for approximations of σ_ϕ^2 and σ_d^2, together with a coarse approximation of σ_v^2.

To be specific, firstly we denote $g(\mathbf{q}_n) \triangleq \phi_n$ where $\mathbf{q}_n = [\theta_{1,n}, \cdots, \theta_{K,n}, d_{1,n}, \cdots, d_{K,n}]^T$. Then with the help of first-order Taylor expansion at the estimation $\widehat{\mathbf{q}}_n$, we have

$$
\begin{aligned}
g(\mathbf{q}_n) &\approx g(\widehat{\mathbf{q}}_n) + \frac{\partial g}{\partial \mathbf{q}_n^T}\bigg|_{\mathbf{q}_n = \widehat{\mathbf{q}}_n}(\mathbf{q}_n - \widehat{\mathbf{q}}_n) \\
&= g(\widehat{\mathbf{q}}_n) + \mathbf{G}_n(\mathbf{q}_n - \widehat{\mathbf{q}}_n),
\end{aligned}
\tag{49}
$$

where $\widehat{\phi}_n = g(\widehat{\mathbf{q}}_n)$, and $\mathbf{G}_n = \frac{\partial g}{\partial \mathbf{q}_n^T}\big|_{\mathbf{q}_n=\widehat{\mathbf{q}}_n} \in \mathbb{R}^{1 \times 2K}$ denote the Jacobian matrix of the angle with respect to $\mathbf{q}_n$. Here, it is a row vector with the form as

$$
\mathbf{G}_n = \left[\frac{\partial g}{\partial \theta_{1,n}}, \cdots, \frac{\partial g}{\partial \theta_{K,n}}, \frac{\partial g}{\partial d_{1,n}}, \cdots, \frac{\partial g}{\partial d_{K,n}}\right]_{\mathbf{q}_n=\widehat{\mathbf{q}}_n}.
\tag{50}
$$

Now, for brief notations, we denote

$$
\Delta X = \sum_{k=1}^{K} d_{k,n} \cos \theta_{k,n} + K\Delta x,
\tag{51}
$$

$$
\Delta Y = \sum_{k=1}^{K} d_{k,n} \sin \theta_{k,n} + K\Delta y.
\tag{52}
$$

Hence, the elements of (50) are derived as

$$
\frac{\partial g}{\partial \theta_{k',n}} = \frac{d_{k',n}\cos\theta_{k',n}\Delta X + d_{k',n}\sin\theta_{k',n}\Delta Y}{\Delta X^2 + \Delta Y^2},
\tag{53}
$$

$$
\frac{\partial g}{\partial d_{k',n}} = \frac{\sin\theta_{k',n}\Delta X - \cos\theta_{k',n}\Delta Y}{\Delta X^2 + \Delta Y^2}.
\tag{54}
$$

Next, a reformulation of (49) is thus obtained as

$$
g(\widehat{\mathbf{q}}_n) \approx g(\mathbf{q}_n) + \mathbf{G}_n\left(\widehat{\mathbf{q}}_n - \mathbf{q}_n\right).
\tag{55}
$$

Now, given $\widehat{\mathbf{q}}_n \sim \mathcal{N}(\mathbf{q}_n, \mathbf{\Sigma}_n)$, it is able to approximate $g(\widehat{\mathbf{q}}_n) \sim \mathcal{N}\left(g(\mathbf{q}_n), \mathbf{G}_n\mathbf{\Sigma}_n\mathbf{G}_n^T\right)$. Since the elements of $\mathbf{q}_n$ are independent of each other, then we have

$$
\mathbf{\Sigma}_n = \mathrm{diag}\left(\sigma_{1,n}^2(1), \cdots, \sigma_{K,n}^2(1), \sigma_{1,n}^2(2), \cdots, \sigma_{K,n}^2(2)\right).
\tag{56}
$$

Finally, the angle variance of the CR is able to be approximated as

$$
\sigma_\phi^2 \approx \mathbf{G}_n\mathbf{\Sigma}_n\mathbf{G}_n^T.
\tag{57}
$$

Similarly, we denote $f(\mathbf{q}_n) \approx f(\widehat{\mathbf{q}}_n) + \mathbf{F}_n(\mathbf{q}_n - \widehat{\mathbf{q}}_n)$, where $f(\mathbf{q}_n) \triangleq d_n$, and $\mathbf{F}_n = \frac{\partial f}{\partial \mathbf{q}_n^T}\big|_{\mathbf{q}_n=\widehat{\mathbf{q}}_n} \in \mathbb{R}^{1 \times 2K}$ denotes the Jacobian matrix of the distance with respect to $\mathbf{q}_n$, which has a similar form as $\mathbf{G}_n$. Hence, the elements of $\mathbf{F}_n$ are derived as

$$
\frac{\partial f}{\partial \theta_{k',n}} = \frac{-d_{k',n}\sin\theta_{k',n}\Delta X + d_{k',n}\cos\theta_{k',n}\Delta Y}{K\sqrt{\Delta X^2 + \Delta Y^2}},
\tag{58}
$$

$$
\frac{\partial f}{\partial d_{k',n}} = \frac{\cos\theta_{k',n}\Delta X + \sin\theta_{k',n}\Delta Y}{K\sqrt{\Delta X^2 + \Delta Y^2}}.
\tag{59}
$$

Finally, the distance variance of CR is able to be approximated as

$$
\sigma_d^2 \approx \mathbf{F}_n\mathbf{\Sigma}_n\mathbf{F}_n^T.
\tag{60}
$$

As for the approximation of σ_v^2, it can not be conducted with the first-order Taylor expansion due to $v_n \neq \frac{c}{2f_c} \cdot \frac{\sum_{k=1}^{K} \mu_{k,n}\cos(\theta_{k,n})/\sigma_{k,n}^2(3)}{\sum_{k=1}^{K}\cos^2(\theta_{k,n})/\sigma_{k,n}^2(3)}$. However, we have noticed that $\widehat{v}_{n|\theta_n} \sim \mathcal{N}\left(v_n, \left(\mathbf{A}^T(\theta_n)\mathbf{Q}_\mu^{-1}\mathbf{A}(\theta_n)\right)^{-1}\right)$, which is based on the assumption of known θ_n. In fact, simulations demonstrate that the approximated accuracy of σ_v^2 has little impact on the performance of beam tracking. Therefore, we may instead use a coarse approximation as

$$
\sigma_v^2 \approx \left(\mathbf{A}^T(\widehat{\theta}_n)\mathbf{Q}_\mu^{-1}\mathbf{A}(\widehat{\theta}_n)\right)^{-1}.
\tag{61}
$$

REFERENCES

[1] Z. Du, F. Liu, and Z. Zhang, "Sensing-assisted beam tracking in V2I networks: Extended target case," in *IEEE International Conference on Acoustics, Speech and Signal Processing (ICASSP)*. IEEE, 2022, pp. 8727–8731.

[2] G. Dimitrakopoulos and P. Demestichas, "Intelligent transportation systems," *IEEE Vehicular Tech Mag*, vol. 5, no. 1, pp. 77–84, 2010.

[3] X. Zhang, S. Hao, R. Wenge, and D. E. Cooper, "Intelligent transportation systems for smart cities: a progress review," *Science China*, vol. 55, no. 012, pp. 2908–2914, 2012.

[4] J. Zhang, F. Wang, K. Wang, W. Lin, X. Xu, and C. Chen, "Data-driven intelligent transportation systems: A survey," *IEEE Trans. Intell. Transp. Syst*, vol. 12, no. 4, pp. 1624–1639, 2011.

[5] J. B. Kenney, "Dedicated short-range communications (DSRC) standards in the United States," *Proc. IEEE*, vol. 99, no. 7, pp. 1162–1182, 2011.

[6] M. Gonzalez-Martín, M. Sepulcre, R. Molina-Masegosa, and J. Gozalvez, "Analytical models of the performance of C-V2X mode 4 vehicular communications," *IEEE Trans. Veh Tech*, vol. 68, no. 2, pp. 1155–1166, 2019.

[7] J. Choi, V. Va, N. Gonzalez-Prelcic, R. Daniels, C. R. Bhat, and R. W. Heath, "Millimeter-wave vehicular communication to support massive automotive sensing," *IEEE Commun Mag*, vol. 54, no. 12, pp. 160–167, 2016.

[8] K. Abboud, H. A. Omar, and W. Zhuang, "Interworking of DSRC and cellular network technologies for V2X communications: A survey," *IEEE Trans. Vehi Tech*, vol. 65, no. 12, pp. 9457–9470, 2016.

[9] Z. Xiao and Y. Zeng, "An overview on integrated localization and communication towards 6G," *Science China Information Sciences*, vol. 65, no. 3, pp. 1–46, 2022.

[10] H. Wymeersch, G. Seco-Granados, G. Destino, D. Dardari, and F. Tufvesson, "5G mmwave positioning for vehicular networks," *IEEE Wireless Commun*, vol. 24, no. 6, pp. 80–86, 2017.

[11] F. Liu, Y. Cui, C. Masouros, J. Xu, T. X. Han, Y. C. Eldar, and S. Buzzi, "Integrated sensing and communications: Towards dual-functional wireless networks for 6G and beyond," *IEEE J. Sel Areas. Commun*, 2022.

[12] A. Liu, Z. Huang, M. Li, Y. Wan, W. Li, T. X. Han, C. Liu, R. Du, D. K. P. Tan, J. Lu *et al.*, "A survey on fundamental limits of integrated sensing and communication," *IEEE Commun. Surveys Tuts*, 2022.

[13] Y. Cui, F. Liu, X. Jing, and J. Mu, "Integrating sensing and communications for ubiquitous IoT: Applications, trends, and challenges," *IEEE Network*, vol. 35, no. 5, pp. 158–167, 2021.

[14] X. Tong, Z. Zhang, J. Wang, C. Huang, and M. Debbah, "Joint multi-user communication and sensing exploiting both signal and environment sparsity," *IEEE J. Sel. Topic. Signal Process*, vol. 15, no. 6, pp. 1409–1422, 2021.

[15] N. González-Prelcic, R. Méndez-Rial, and R. W. Heath, "Radar aided beam alignment in mmwave V2I communications supporting antenna diversity," in *2016 Information Theory and Applications Workshop (ITA)*. IEEE, 2016, pp. 1–7.

[16] F. Liu, W. Yuan, C. Masouros, and J. Yuan, "Radar-assisted predictive beamforming for vehicular links: Communication served by sensing," *IEEE Trans. Wireless Commun*, vol. 19, no. 11, pp. 7704–7719, 2020.

[17] W. Yuan, F. Liu, C. Masouros, J. Yuan, D. W. K. Ng, and N. González-Prelcic, "Bayesian predictive beamforming for vehicular networks: A low-overhead joint radar-communication approach," *IEEE Trans. Wireless Commun*, vol. 20, no. 3, pp. 1442–1456, 2020.

[18] F. Liu and C. Masouros, "A tutorial on joint radar and communication transmission for vehicular networks-part i: Background and fundamentals," *IEEE Commun. Lett*, 2020.

[19] ——, "A tutorial on joint radar and communication transmission for vehicular networks-part ii: State of the art and challenges ahead," *IEEE Commun. Lett*, 2020.

[20] ——, "A tutorial on joint radar and communication transmission for vehicular networks-part iii: Predictive beamforming without state models," *IEEE Commun. Lett*, 2020.

[21] M. A. Richards, *Fundamentals of radar signal processing*. McGraw-Hill Education, 2014.

[22] J. Wang, Z. Lan, C.-w. Pyo, T. Baykas, C.-s. Sum, M. A. Rahman, J. Gao, R. Funada, F. Kojima, and H. Harada, "Beam codebook based beamforming protocol for multi-Gbps millimeter-wave WPAN systems," *IEEE J. Sel Areas. Commun*, vol. 27, no. 8, pp. 1390–1399, 2009.

[23] D. Zhang, A. Li, M. Shirvanimoghaddam, P. Cheng, Y. Li, and B. Vucetic, "Codebook-based training beam sequence design for millimeter-wave tracking systems," *IEEE Trans. Wireless Commun*, vol. 18, no. 11, pp. 5333–5349, 2019.

[24] D. Zhu, J. Choi, and R. W. Heath, "Auxiliary beam pair enabled AoD and AoA estimation in closed-loop large-scale millimeter-wave MIMO systems," *IEEE Trans. Wireless Commun*, vol. 16, no. 7, pp. 4770–4785, 2017.

[25] F. Liu, P. Zhao, and Z. Wang, "EKF-based beam tracking for mmwave MIMO systems," *IEEE Commun. Lett*, vol. 23, no. 12, pp. 2390–2393, 2019.

[26] E. Dahlman, S. Parkvall, and J. Skold, *5G NR: The next generation wireless access technology*. Academic Press, 2020.

[27] X. Meng, F. Liu, C. Masouros, W. Yuan, Q. Zhang, and Z. Feng, "Vehicular connectivity on complex trajectories: Roadway-geometry aware isac beam-tracking," *arXiv:2205.11749*, 2022.

[28] W. Yi, T. Zhou, Y. Ai, and R. S. Blum, "Suboptimal low complexity joint multi-target detection and localization for non-coherent MIMO radar with widely separated antennas," *IEEE Trans. Signal Process*, vol. 68, pp. 901–916, 2020.

[29] S. Kay, *Fundamentals of Statistical Signal Processing, Vol. I: Estimation Theory*. Upper Saddle River, NJ: Prentice-Hall PTR, 1993.

[30] M. Keskin, H. Wymeersch, and V. Koivunen, "ICI-aware parameter estimation for MIMO-OFDM radar via APES spatial filtering," in *ICASSP 2021-2021 IEEE International Conference on Acoustics, Speech and Signal Processing (ICASSP)*. IEEE, 2021, pp. 8248–8252.

[31] R. Faragher, "Understanding the basis of the kalman filter via a simple and intuitive derivation [lecture notes]," *IEEE Signal Process. Mag*, vol. 29, no. 5, pp. 128–132, 2012.

[32] D. J. Salmond and M. C. Parr, "Track maintenance using measurements of target extent," *IEE Proceedings-Radar, Sonar and Navigation*, vol. 150, no. 6, pp. 389–395, 2003.

[33] H. Godrich, V. M. Chiriac, A. M. Haimovich, and R. S. Blum, "Target tracking in MIMO radar systems: Techniques and performance analysis," in *2010 IEEE Radar Conference*. IEEE, 2010, pp. 1111–1116.

[34] Z. Zhong, H. Meng, and X. Wang, "A comparison of posterior cramer–rao bounds for point and extended target tracking," *IEEE Signal Process. Lett*, vol. 17, no. 10, pp. 819–822, 2010.

[35] L. Liu, S. Zhang, and R. Zhang, "CoMP in the sky: UAV placement and movement optimization for multi-user communications," *IEEE Trans. Commun*, vol. 67, no. 8, pp. 5645–5658, 2019.

[36] X. Song, S. Haghighatshoar, and G. Caire, "Efficient beam alignment for millimeter wave single-carrier systems with hybrid MIMO transceivers," *IEEE Trans. Wireless Commun*, vol. 18, no. 3, pp. 1518–1533, 2019.

[37] H. L. Van Trees, *Optimum array processing: Part IV of detection, estimation, and modulation theory*. John Wiley & Sons, 2004.

[38] S. Boyd and L. Vandenberghe, *Convex optimization*. Cambridge university press, 2004.

Zhen Du received the B.Eng. degree in communication engineering from Northwestern Polytechnical University, Xi'an, China, in 2016 and the Ph.D. degree in information and communication engineering from Shanghai Jiao Tong University, Shanghai, China, in 2022. From June 2021 to May 2022, he was a visiting researcher with the Department of Electrical and Electronic Engineering, Southern University of Science and Technology, Shenzhen, China. Since September 2022, he has been a lecturer with the School of Electronic and Information Engineering, Nanjing University of Information Science and Technology, Nanjing, China. His research interests include integrated sensing and communication (ISAC) systems, beam management in vehicular networks, and radar signal processing.

Fan Liu (Member, IEEE) is currently an Assistant Professor of the Department of Electrical and Electronic Engineering, Southern University of Science and Technology (SUSTech). He received the Ph.D. and the BEng. degrees from Beijing Institute of Technology (BIT), Beijing, China, in 2018 and 2013, respectively. He has previously held academic positions in the University College London (UCL), UK, first as a Visiting Researcher from 2016 to 2018, and then as a Marie Curie Research Fellow from 2018 to 2020.

Dr. Fan Liu's research interests lie in the general area of signal processing and wireless communications, and in particular in the area of Integrated Sensing and Communications (ISAC). He has 10 publications selected as IEEE ComSoc Besting Readings in ISAC. He is the Founding Academic Chair of the IEEE ComSoc ISAC Emerging Technology Initiative (ISAC-ETI), an Associate Editor for the IEEE Communications Letters and the IEEE Open Journal of Signal Processing, and a Guest Editor of the IEEE Journal on Selected Areas in Communications, IEEE Wireless Communications, and China Communications. He was also an organizer and Co-Chair for numerous workshops, special sessions and tutorials in flagship IEEE/ACM conferences, including ICC, GLOBECOM, ICASSP, and MobiCom. He is the TPC Co-Chair of the 2nd and 3rd IEEE Joint Communication and Sensing Symposium (JC&S), and will serve as a Track Co-Chair for the IEEE WCNC 2024. He is a Member of the IMT-2030 (6G) ISAC Task Group. He was the recipient of the IEEE Signal Processing Society Young Author Best Paper Award of 2021, the Best Ph.D. Thesis Award of Chinese Institute of Electronics of 2019, the EU Marie Curie Individual Fellowship in 2018, and has been named as an Exemplary Reviewer for IEEE TWC/TCOM/COMML for 5 times. Dr. Fan Liu was listed in the World's Top 2% Scientists by Stanford University for citation impact in 2021 and 2022.

Christos Masouros (Senior Member, IEEE) received the Diploma degree in electrical and computer engineering from the University of Patras, Greece, in 2004, and the M.Sc. by research and Ph.D. degrees in electrical and electronic engineering from The University of Manchester, U.K., in 2006 and 2009, respectively. In 2008, he was a Research Intern at Philips Research Labs, U.K. Between 2009 and 2010, he was a Research Associate with The University of Manchester and a Research Fellow at Queen?s University Belfast between 2010 and 2012. In 2012, he joined University College London as a Lecturer. He has held a Royal Academy of Engineering Research Fellowship between 2011 and 2016. Since 2019, he has been a Full Professor of signal processing and wireless communications with the Information and Communication Engineering Research Group, Department of Electrical and Electronic Engineering, and affiliated with the Institute for Communications and Connected Systems, University College London. His research interests lie in the field of wireless communications and signal processing with particular focus on green communications, large scale antenna systems, integrated sensing and communications, interference mitigation techniques for MIMO, and multicarrier communications. He was the co-recipient of the 2021 IEEE SPS Young Author Best Paper Award. He was the recipient of the Best Paper Awards in the IEEE GlobeCom 2015 and IEEE WCNC 2019 conferences, and has been recognized as an Exemplary Editor for the IEEE COMMUNICATIONS LETTERS and as an Exemplary Reviewer for the IEEE TRANSACTIONS ON COMMUNICATIONS. He is a founding member and the Vice-Chair of the IEEE Emerging Technology Initiative on Integrated Sensing and Communications, the Vice Chair of the IEEE Special Interest Group on Integrated Sensing and Communications (ISAC), and the Chair of the IEEE Special Interest Group on Energy Harvesting Communication Networks. He is an Editor of IEEE TRANSACTIONS ON COMMUNICATIONS, IEEE TRANSACTIONS ON WIRELESS COMMUNICATIONS, the IEEE OPEN JOURNAL OF SIGNAL PROCESSING; and the Editor-at-Large of IEEE OPEN JOURNAL OF THE COMMUNICATIONS SOCIETY. He has been an Associate Editor of IEEE COMMUNICATIONS LETTERS and a Guest Editor for a number of IEEE JOURNAL OF SELECTED TOPICS IN SIGNAL PROCESSING and IEEE JOURNAL ON SELECTED AREAS IN COMMUNICATIONS issues.

Weijie Yuan (Member, IEEE) received the B.S. degree from Beijing Institute of Technology, Beijing, China, in 2013, and the Ph.D. degrees from Beijing Institute of Technology, Beijing, China, and the University of Technology Sydney, Ultimo, NSW, Australia, in 2019. He was a Visiting Researcher with Vienna University of Technology, a Research Assistant with the University of Sydney, a Visiting Associate Fellow with the University of Wollongong, and a Visiting Fellow with the University of Southampton, Southampton, U.K., from 2016 to 2019. He was a Research Associate with the University of New South Wales, Sydney, NSW, Australia, from 2019 to 2021. He is currently an Assistant Professor with the Department of Electrical and Electronic Engineering, Southern University of Science and Technology, Shenzhen, China.

Dr. Yuan was a recipient of the Best Ph.D. Thesis Award from the Chinese Institute of Electronics and the Exemplary Reviewer from the IEEE TRANSACTIONS ON COMMUNICATIONS/IEEE WIRELESS COMMUNICATIONS LETTERS. He was an Organizer/Chair of several workshops and special sessions on orthogonal time frequency space (OTFS) and integrated sensing and communication in flagship IEEE and ACM conferences, including IEEE ICC, IEEE/CIC ICCC, IEEE SPAWC, IEEE VTC, IEEE WCNC, IEEE ICASSP, and ACM MobiCom. He is the Founding Chair of the IEEE ComSoc Special Interest Group on OTFS. He currently serves as an Associate Editor for the IEEE COMMUNICATIONS LETTERS, and an Associate Editor and an Award Committee Member for the EURASIP Journal on Advances in Signal Processing. He has led the guest editorial teams for three special issues in the IEEE Communications Magazine, IEEE TRANSACTIONS ON GREEN COMMUNICATIONS AND NETWORKING, and China Communications. Dr. Yuan was listed in the World's Top 2% Scientists by Stanford University for citation impact in 2022.

Zenghui Zhang (Senior Member, IEEE) received the B.Sc. degree in applied mathematics, the M.Sc. degree in computational mathematics, and the Ph.D. degree in information and communication engineering from the National University of Defense Technology, Changsha, China, in 2001, 2003, and 2008, respectively. From 2008 to 2012, he was a Lecturer with the Department of Mathematics and System Science, National University of Defense Technology. In 2013, he joined Shanghai Jiao Tong University, Shanghai, China, where he is currently a Professor with the School of Electronic Information and Electrical Engineering. His research interests include radar signal processing, microwave imaging, SAR image interpretation, target detection, and recognition. In these areas, he has published more than 100 research articles.

Shuqiang Xia is a senior communication research expert in ZTE. His research interests focus on Integrated Sensing and Communications (ISAC), carrier aggregation (CA), and Ultra-Reliable Low-Latency Communications (URLLC). He received his master's degree in signal and information processing from Nanjing University of Science and Technology, China, in 2002. He was a recipient of the China Patent Gold Award and Second Prize of National Technological Invention Award.

Giuseppe Caire (Fellow, IEEE) was born in Torino in 1965. He received a B.Sc. in Electrical Engineering from Politecnico di Torino in 1990, an M.Sc. in Electrical Engineering from Princeton University in 1992, and a Ph.D. from Politecnico di Torino in 1994. He has been a post-doctoral research fellow with the European Space Agency (ESTEC, Noordwijk, The Netherlands) in 1994-1995, Assistant Professor in Telecommunications at the Politecnico di Torino, Associate Professor at the University of Parma, Italy, Professor with the Department of Mobile Communications at the Eurecom Institute, Sophia-Antipolis, France, a Professor of Electrical Engineering with the Viterbi School of Engineering, University of Southern California, Los Angeles, and he is currently an Alexander von Humboldt Professor with the Faculty of Electrical Engineering and Computer Science at the Technical University of Berlin, Germany.

He received the Jack Neubauer Best System Paper Award from the IEEE Vehicular Technology Society in 2003, the IEEE Communications Society and Information Theory Society Joint Paper Award in 2004 and in 2011, the Okawa Research Award in 2006, the Alexander von Humboldt Professorship in 2014, the Vodafone Innovation Prize in 2015, an ERC Advanced Grant in 2018, the Leonard G. Abraham Prize for best IEEE JSAC paper in 2019, the IEEE Communications Society Edwin Howard Armstrong Achievement Award in 2020, and he is a recipient of the 2021 Leibniz Prize of the German National Science Foundation (DFG). Giuseppe Caire is a Fellow of IEEE since 2005. He has served in the Board of Governors of the IEEE Information Theory Society from 2004 to 2007, and as officer from 2008 to 2013. He was President of the IEEE Information Theory Society in 2011. His main research interests are in the field of communications theory, information theory, channel and source coding with particular focus on wireless communications.